Geopersia 2026, 16(1): 33-68
DOI: 10.22059/geope.2025.393863.648816

RESEARCH PAPER

Petrography, mineral chemistry and geothermobarometry of monzogabbro-monzodiorite intrusions of N-NE Bafq: An approach to understanding of the Ediacaran-Cambrian intracontinental rift in the central part of Iran

Foroogh Zolala [1], Mahmood Sadeghain [1], *, Masood Alipour-Asll [1], Lambrini Papadopoulou [2], Zhai Mingguo [3], Foteini Aravani [2], Xiyan Zhu [3]

[1] Petrology and Economic Geology Department, Shahrood University of Technology, Shahrood, Iran
[2] Department of Mineralogy-Petrology-Economic Geology, School of Geology, Aristotle University, Greece
[3] Institute of Geology and Geophysics, Chinese Academy of Sciences (CAS), China

Received: 21 April 2025, Revised: 10 June 2025, Accepted: 14 July 2025

Abstract
The study area is located in the N-NE Bafq and the central Iran structural zone. The Rizu-Desu volcano-sedimentary sequence is crosscut by bimodal (basic and felsic) intrusions and dikes, with compositions ranging from monzogabbro to leucogranite. In the monzogabbro-monzodiorite intrusions (540 to 520 Ma) of the investigated region, plagioclase (with a dominant albite-oligoclase composition), pyroxene (diopside and augite), Ca-Fe-Ti-rich amphiboles (magnesiohornblende, tschermakite, Kaersutite, and ferrokaersutite), and biotite (Fe-biotite, Mg-biotite, and also Ti-rich (0.38-1)) are the essential minerals. Apatite, monazite, magnetite, titanomagnetite, titanite (sphene), and zircon are also accessory minerals. Geothermobarometry investigations based on the mineral chemistry of pyroxene, amphibole, and biotite indicate the temperatures of cessation of exchange and final equilibrium of the minerals, mainly covering a temperature range of 1270 to 1140 °C (pyroxenes), 890-790 °C (amphiboles) and 780-745 °C (biotites) (in respectively) and the pressure mainly cover range of 12.33 to 0.5 kbar. Petrological features of the studied rocks are very similar to those of appinite rocks. The parental magmas of monzogabbro-monzodiorite intrusions have been mostly alkaline nature and originated from partial melting of the metasomatized mantle source in an intracontinental rift tectonic setting. The resulting magmas evolved by fractional crystallization, and possibly crustal contamination, then emplaced in the continental crust around Ediacaran-Cambrian boundary.

Keywords: Monzogabbro-Monzodiorite, Mineral Chemistry, Geothermobarometry, Intracontinental Rift, Bafq.

Introduction

The geological history of Iran records many events, from the Precambrian to the present, which demonstrate a sequence of processes that have taken place in different geological environments. One of the most notable occurrences is intracontinental rifting, which took place at the boundary Ediacaran - Cambrian. The evidence of rifting is preserved in certain regions of Central Iran and the Zagros structural zones. Rizu, Desu (Dezu), Ravar, and Hormuz series are well-documented intracontinental rift-related sequences. Across an area exceeding one thousand square kilometers in the N-NE Bafq, the Rizu-Desu series consists of volcano-sedimentary

* Corresponding author e-mail: Sadeghian.petrology@gmail.com

sequences. These sequences include multiple small-scale igneous bodies up to stock-sized intrusions. Those are distinguished by bimodal lithological compositions. This area includes world-class substantial reserves of iron, iron-apatite, lead, zinc, manganese, uranium, and rare earth minerals. This research focuses on a specific subset consisting of gabbro, monzogabbro, monzodiorite and gabbro-diorite, collectively referred to as monzogabbro-monzodiorite. An examination of the petrography, mineral chemistry, and geothermobarometry of these monzogabbro-monzodiorite rocks is conducted to provide a greater understanding of the rifting processes associated with their formation.

Geothermobarometry of igneous rocks is a fundamental aspect of petrological studies, relying principally on the chemical composition of key minerals such as pyroxene, amphibole, and biotite. Amphibole and pyroxene are some of the most common mafic minerals in igneous rocks, such as gabbro, diorite, and granodiorite, and play a crucial role in the understanding of geobarometry conditions. A significant amount of research has been conducted by numerous investigators into the use of these minerals in geothermobarometric studies, leading to a considerable collection of published studies. Specialized software tools have been developed and further refined to improve the efficiency and accuracy of these analyses (Morimoto, 1988; Soesoo, 1997; Berger et al., 2005; Putirka, 2008; Putirka, 2016; Ridolfi et al., 2018; Ridolfi, 2021; etc.).

The majority of geological research conducted in the N-NE Bafq area, focused on the igneous rocks and mineral deposits, has been primarily based on geochemical and isotopic analyses of the whole rock samples (e.g., Poshtkoohi et al., 2018; Majidi et al., 2021; Mehdipour-Ghazi, 2021). Investigations focusing on mineral chemistry were typically limited to examining only ore minerals within mineralized zones. Consequently, no prior study has systematically investigated the mineral chemistry of the N-NE Bafq intrusions. This article represents the first comprehensive research to examine these rocks from a geothermobarometric point of view, utilizing detailed mineral chemical analyses. Notable studies that have explored mineral chemistry in the context of mineralization or ore minerals include Sepidbar et al., 2021; Torab and Lehmann, 2007; Teymouri et al., 2022; Hafezian & Jamali, 2015; Sepehri-Rad et al., 2018; Salami et al., 2021; and Zolala et al., 2025.

Geological setting

The study area is located within the Central Iran structural zone (Aghanabati, 2004), where the oldest exposed rocks belong to the Precambrian metamorphic basement, including the Sarhad, Neden, and Natk complexes (Ramezani & Tucker, 2003; Masoudi et al., 2008) (figure 1). These basement rocks, in various geological maps (Soheili & Mahdavi, 1991; Amini et al., 2004; Majidi & Babakhani, 2000; Ghaemi & Saeedi, 2006), consist of metapelites (phyllite, micaschist, garnet-mica schists, staurolite-garnet-mica schists, garnet-andalusite schist, garnet-Kyanite schist, graphite schist), metasandstones (metapsammites), metacarbonates (marbles), and metabasites (greenschists, amphibole schists, amphibolites, garnet-amphibolites), along with migmatites and granitoids (Majidi & Babakhani, 2000; Ghaemi & Saeedi, 2006, Mehdipour-Ghazi et al., 2021). This region hosts significant iron mineralization occurrences, including layered and massive deposits associated with the metamorphic rocks (Lotfi et al., 1998). Notable examples include the Gelmandeh iron deposit northeast of Saghand (associated with garnet amphibolite), southwest of Robat-e-Posht-e-Badam (the Robat iron mine), and iron ore indications in the Zaman Abad area. Similar iron mineralization has been reported from the south-southeast of the Shahrood (Khartouran area), iron ore indications associated with the Majerad and Do Chah metamorphic complexes (Veiskarami, 2018; Rezaei, 2020), as well as the Narm and Tengal Sefid deposits southwest of Bardaskan (Parvaresh-Darbandi, 2020). Recent researches include iron-manganese occurrences south of Damghan and northwest of

Moalleman (Hassanzadeh & Ghorbani, personal communication). Zarshouran (North of Takab) and Muteh (northeast of Golpayegan) gold deposits, and also the Angouran lead and zinc deposit (west of Zanjan or northwestof Takab), can be added to this collection (see figure 2 and table 1).

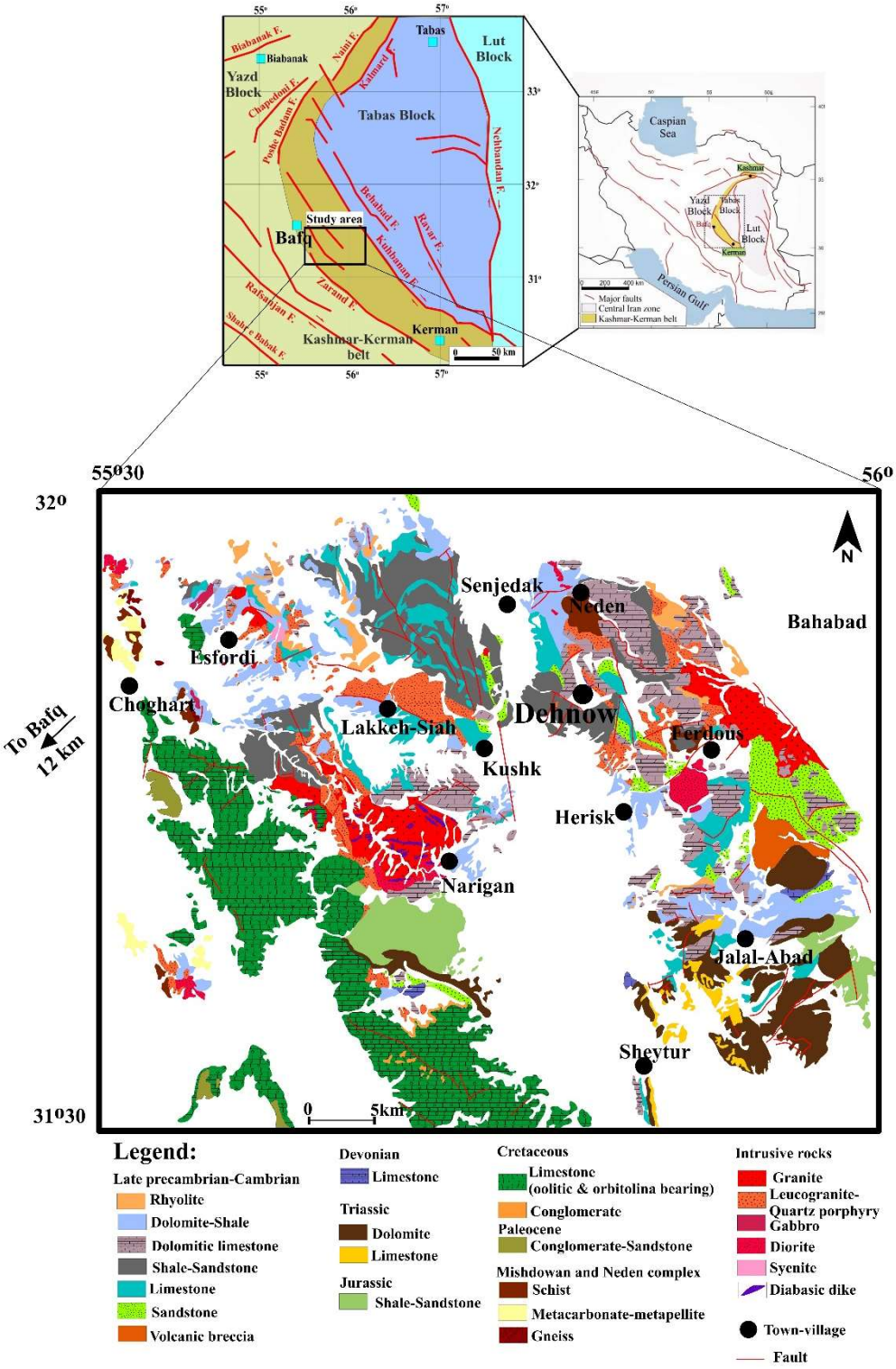

Figure 1. Geological map of the study area

Table 1. Some of the late Neoproterozoic ore deposits or ore indications of Iran

No	Location or name of the ore deposit	Nearest city or village	X	Y
1	Chah-Farakh Copper deposit (In the exploration stage, to start mining operations)	South of Damghan	249169	3923202
2	Chah-Farakh Copper deposit (In the exploration stage, to start mining operations)	South of Damghan	251146	3923773
3	Halalan Mn mine (No I) (semi-active mine)	South of Damghan	261598	3907059
4	Halalan Mn mine (No II) (semi-active mine or not fully operational)	South of Damghan	262809	3907266
5	Sorkhtool iron ore indication	Southeast of Shahrood	384364	3954528
6	Par O Bal iron ore indication	Southeast of Shahrood	394105	3955252
7	Majerad iron ore indications	Southeast of Shahrood	415102	3964624
8	Narm iron ore deposits	southwest of Bardaskan	534495	3858723
9	Tengel Sefid iron ore deposits (mine in operation)	southwest of Bardaskan	573612	3872502
10	Robat iron ore deposits (mine in operation)	southwest of Robat – e - Posht Badam	366776	3646507
11	Zaman Abad iron ore deposit (in the exploration stage)	southwest of Robat – e - Posht Badam	369561	3638355
12	Gelmandeh iron deposits (new mine in operation)	northeast of Saghand	355802	3616062
13	Gol-Gohar iron deposit (mine in operation)	southwest of Sirjan	336908	329598
14	Zarshouran gold deposit (mine in operation)	North of Takab	691154	4065924
15	Angouran lead and zinc deposit (mine in operation)	northwest of Zanjan	715202	4055884
16	Muteh gold deposit (mine in operation)	northeast of Golpayegan	478659	3728974

The metamorphic basement is overlain by the Kharangan series, a thick sequence of alternating shale, sandstone, limestone, and basic volcanic rocks (Sabzehei, 2017). Equivalent units include the Morad series in northwest Kerman (Vahdati-e-Daneshmand et al., 1992; Djokovic et al., 1972) and the Kalmard series in the west of Robat-e-Kalmard village (Aghanbati, 2002; Sheikholeslami & Zamani, 1999). These are discontinuously overlain by Ordovician-Silurian carbonates and Permian dolomitic limestones of the Jamal Formation (Griffis et al., 1981).

In the Bafq area, the Kharangan series is overlain by the Precambrian-Lower Cambrian Rizu volcano-sedimentary series (Soheili & Mahdavi, 1991; Sabzehei, 2017). This series include basaltic to rhyolitic lavas, iron-apatite mineralization, and fossiliferous limestones (Vaziri et al., 2019). Similar sequences are known as the Rizu, Desu, Ravar, and Hormuz series in different locations (Pilgrim, 1908; Huckriede et al., 1962; Stocklin, 1968). These represent an Ediacaran-Lower Cambrian rift association related to northern Gondwana, extending from Iran to Oman (Faramarzi et al., 2015). The Rizu series is intruded by bimodal igneous rocks (granite to gabbro) and cut by diabasic dikes (Sadeghian et al., 2017). The Zarigan, Narigan, and Bahabad plutons are notable examples, with Zarigan and Narigan showing extensive dike swarms (e.g., see figures 3, 4, and 5). Unlike the older basement, which underwent Barrovian-type metamorphism (greenschist to amphibolite facies) and intense deformation (Sadeghian et al., 2017), the Rizu-Desu series is not metamorphosed.

Stratigraphic relationships are often faulted, though in NE Zarand this series is overlain clearly by Cambrian Soltaniyeh, Zaygun, and Lalun Formations, followed by Ordovician-Jurassic strata (Sadeghian, field observations). In the Bafq area, the Rizu series is discontinuously covered by Triassic-Cretaceous sediments and Cenozoic deposits (Aghanbati, 2002).

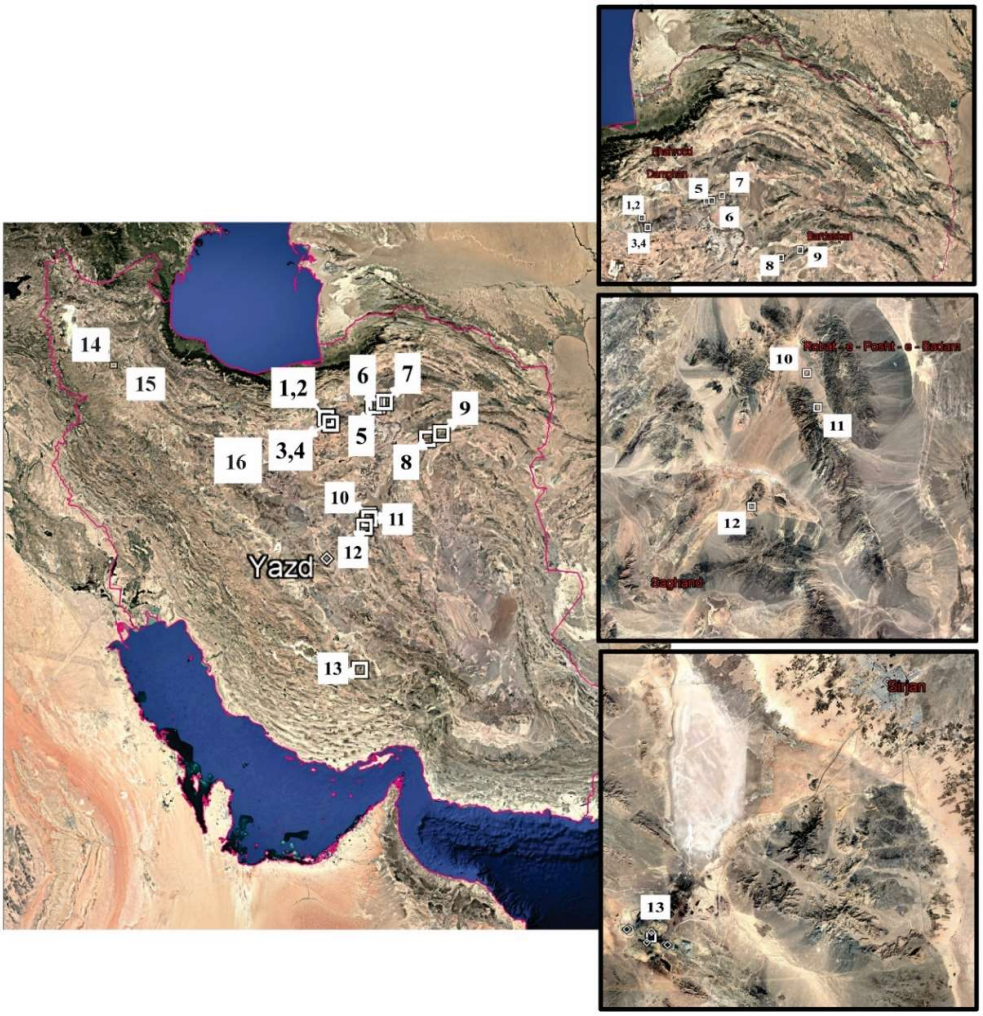

Figure 2. Distribution map of the ore deposits associated with late Neoproterozoic metamorphic rocks of Iran. Detailed information is given in table 1

No.	Ore deposit	No.	Ore deposit
1	Chah-Farakh Copper deposit	9	Tengal Sefid iron ore deposits
2	Chah-Farakh Copper deposit	10	Robat iron ore deposits
3	Halalan Mn mine (No I)	11	Zaman Abad iron ore deposit
4	Halalan Mn mine (No II)	12	Gelmandeh iron deposits
5	Sorkhtool iron ore indication	13	Gol-Gohar iron deposit
6	Par O Bal iron ore indication	14	Zarshouran gold deposit
7	Majerad iron ore indications	15	Angouran lead and zinc deposit
8	Narm iron ore deposits	16	Muteh gold deposit
Detailed information is given in table 1.			

The equivalent Hormuz series in the north of the Persian Gulf contains similar salt-bearing volcano-sedimentary rocks (Ahmadi-Moghadam, 2019; Shahri, 2022). Both Rizu and Hormuz series have Ediacaran-Cambrian ages and bimodal igneous compositions (Pirooj et al., 2019; Asadi-Sarshar, 2020). Despite numerous studies (Heidari, 1996; Sharifi, 1997; Bonyadi, 2011), detailed petrological work on the Rizu-Desu intrusions remains limited. Recent researches, such as Bonyadi., 2005; Bonyadi et al., 2011; Sepehrirad et al., 2018; Sepehri-Rad., 2019 and Sepehrirad & Alirezaei., 2020; Sepidbar et al., 2022 and other researchers, focused on mineral chemistry of mineral assemblages of alteration zones and also determined salinity and homogenization temperatures of the fluids concerning ore deposits, which had an important role in mineralization procedures.

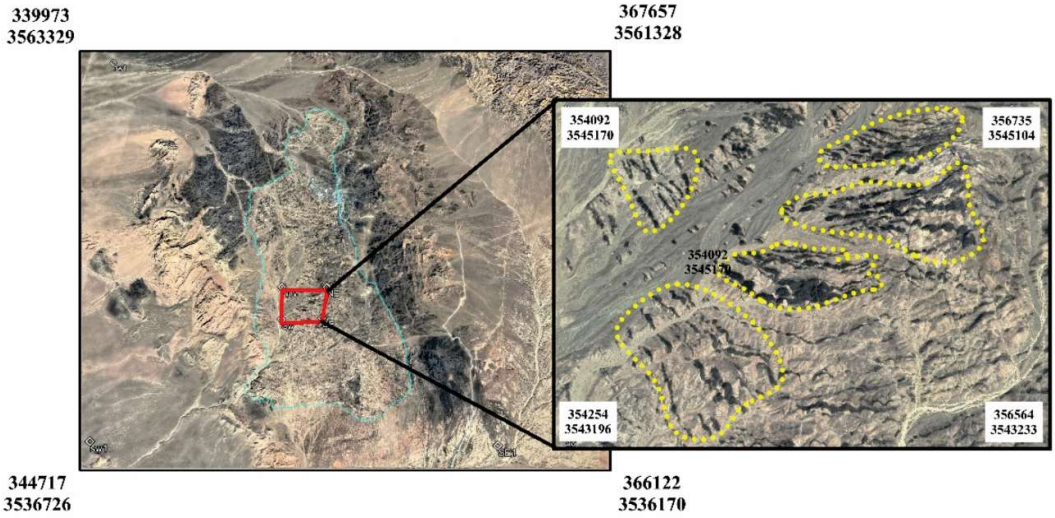

Figure 3. Satellite images of diabasic dike swarms cutting the Zarigan granitoid

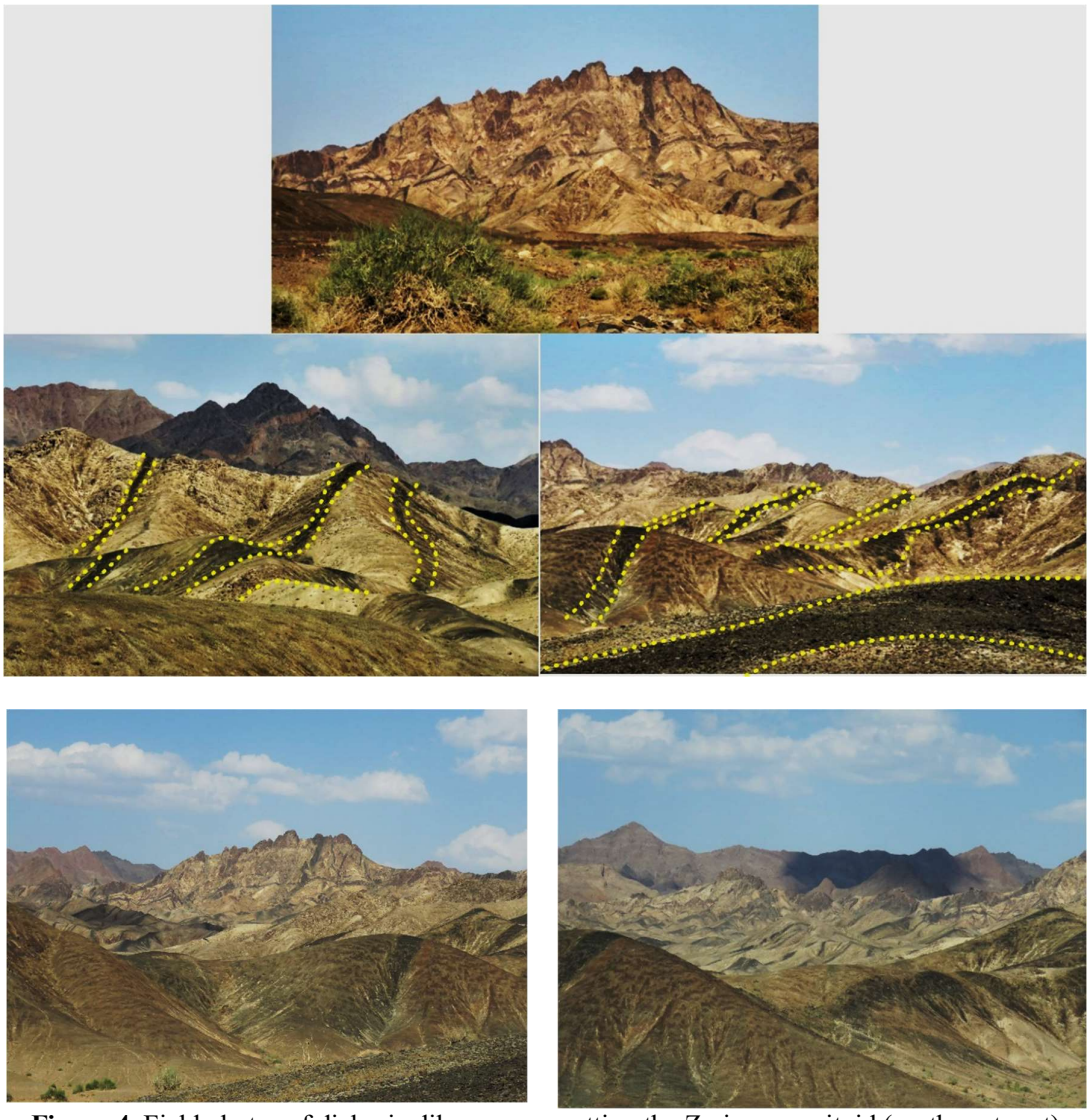

Figure 4. Field photos of diabasic dike swarms cutting the Zarigan granitoid (northwest part)

The Central structural Iran zone thus preserves a wide spectrum of records from Precambrian magmatism and metamorphism to Phanerozoic sedimentation. The Rizu-Desu series and associated intrusions provide critical insights into Gondwana-related tectonics and iron mineralization events. Further petrological and geochemical studies are needed to fully understand the petrogenesis and tectonic evolution of these complexes.

Research methods

To investigate the rock units in the north-northeast Bafq region, over 200 field stations were surveyed, and more than 450 rock samples were collected. These samples were gathered for a range of analytical purposes, including petrographic studies, microprobe and whole rock geochemical analysis, isotopic analysis, and geochronological dating. More than three hundred samples of igneous rocks were collected from the N-NE Bafq region.

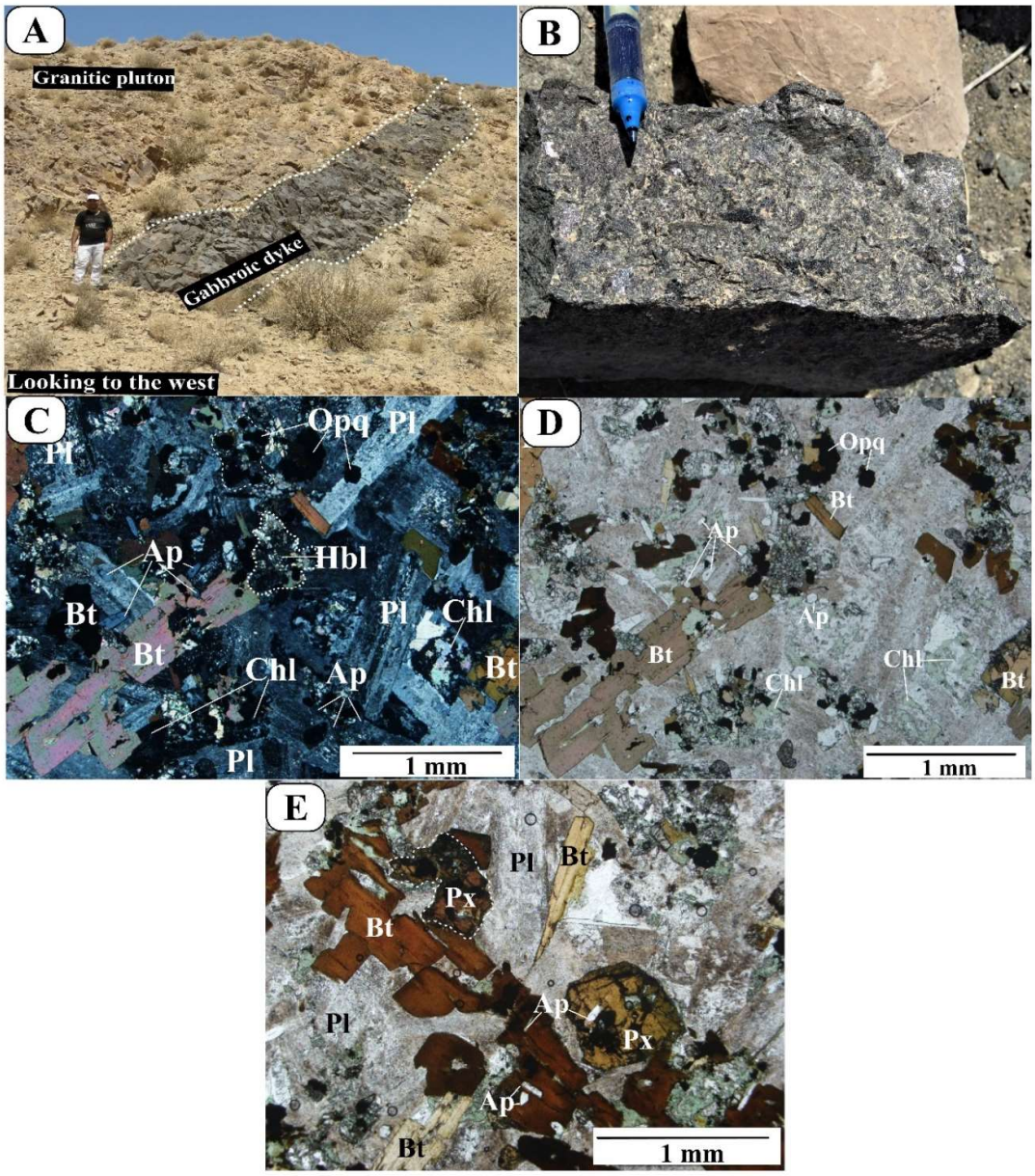

Figure 5. See the caption in the next page. Also, continued in the next page

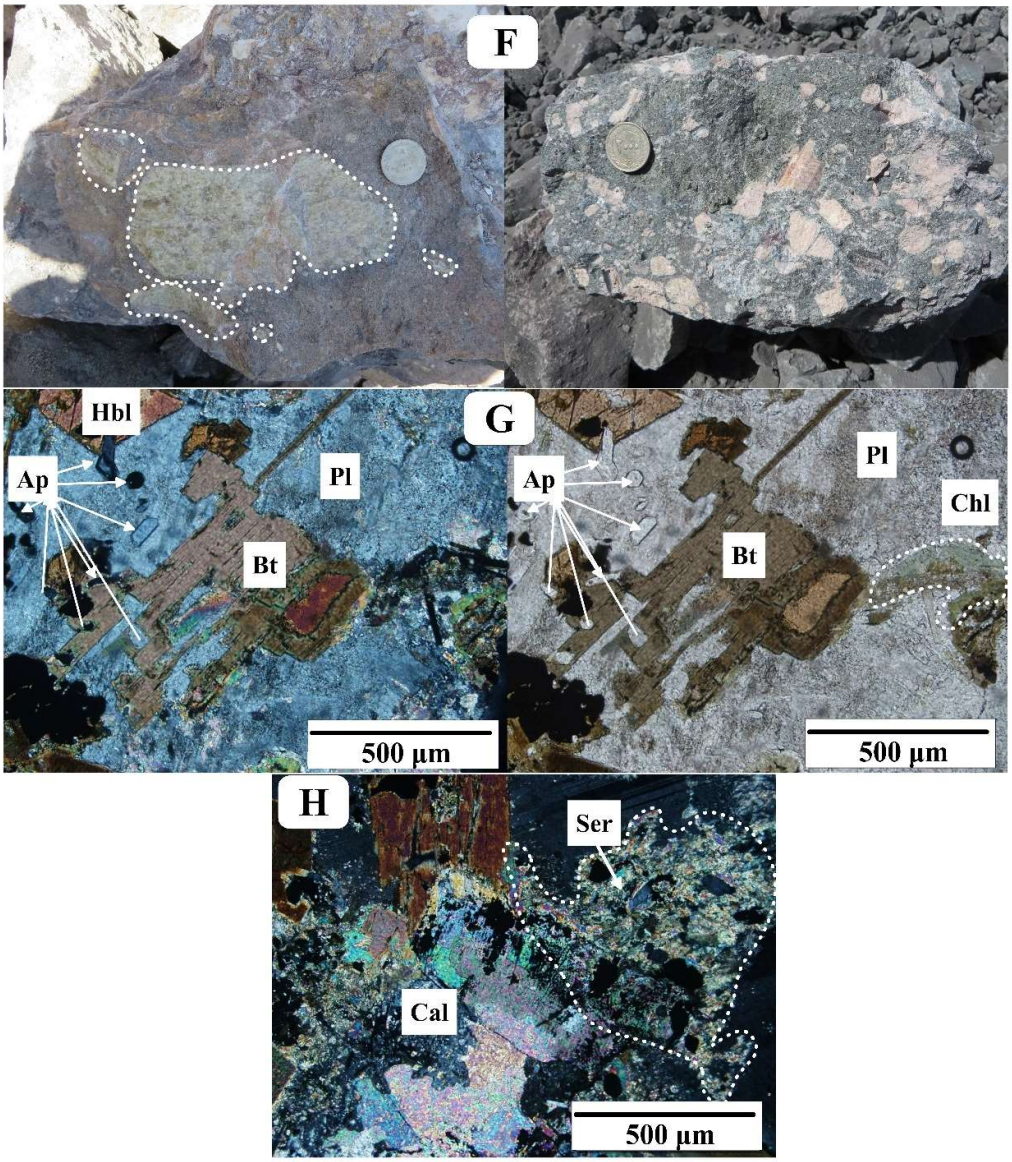

Figure 5. (a) Field photo of the gabbroic dike cut the Narigan granitic pluton (southwest of Narigan village, looking to the west), (b) Hand sample of Narigan biotite-rich monzogabbro, and (c, d & e) Photomicrographs of the investigated monzogabbro-monzodiorites (in XPL & PPL). (f) Large green and pink apatite crystals. (g) Photomicrographs of the investigated monzogabbro-monzodiorites with emphasis on the presence of apatites (in XPL & PPL) plus chloritization. (h) Secondary alteration processes, including sericitization and calcitization

From this collection, three monzogabbro-monzodiorite samples were selected for detailed mineralogical analysis from Narigan (NG-01.2), Dehnow (ZB-15.2) and Esfordi (Esf-gb). Polished thin sections of the selected samples were prepared, marked, and analyzed using by electron microprobe at the scanning electron microscopy laboratory of the Aristotle University of Thessaloniki, Greece. The analyses were conducted using a SEM (JEOL JSM-840A) equipped with an energy dispersive spectrometer (EDS, Oxford INCA 250), operating at an accelerating voltage of 20 kV and a probe current of 0.4 mA. A pure Co standard was employed for EDS calibration. Before SEM observations, the samples were coated with a 200 Å carbon layer using a JEOL-4 × vacuum evaporator. The detection limits ranged between 0.2 and 0.6 wt.%, and the obtained data were processed using various software programs allocated for

specific analytical needs. The results, along with the graphs generated from them, were subsequently utilized for interpretation and analysis. It should be noted that the thermobarometric calculations of amphiboles were performed using an Excel spreadsheet, which was designed by Ridolfi (2021).

Results

Field studies and petrography

In the northern and northeastern Bafq region, encompassing the Esfordi, Narigan, and Dehnow areas, basic to intermediate rocks are exposed predominantly as lava flows, dikes, and small-scale intrusions (including plugs and rarely stocks) (figure 1). The surface exposure of these intrusions ranges from a few square meters to approximately 2 km^2. The 1:25,000 scale geological maps of Aliabad (Sabzehei, 2017), Herisk (Nogol-Sadat, 2012), and Esfeng (Sadeghian, 2018) illustrate the outcrops of numerous mafic to intermediate intrusions. Examples include: monzogabbro-monzodiorites of the north of Esfordi Iron-Apatite mine (covering several tens of square meters), east of Dehnow village (spanning several hundred square meters), and the north of Narigan village (extending over several tens of square meters).

Rocks of these intrusions are medium- to coarse-grained in hand samples or specimens and display black to dark green colors. In most samples, iron- and magnesium-rich silicate minerals (mafic), particularly amphiboles and micas, are distinctly visible in the macroscopic scale. At the microscopic scale, these rocks vary from coarse- to fine-grained (with finer grains typically observed in marginal samples) and exhibit euhedral to subhedral crystal forms. They display granular to intergranular, ophitic, and sub-ophitic textures. The main minerals include clinopyroxene, amphibole (green and brown hornblende), biotite, plagioclase, and a little K-feldspar. Accessory minerals in these rocks include zircon, apatite, sphene (titanite), magnetite, and titanomagnetite (opaque minerals), as well as rare earth element-rich minerals such as monazite and bastnäsite, along with ore minerals of pyrite and chalcopyrite (Zolala et al., 2025). Secondary alteration processes, including sericitization, chloritization, and calcitization, are also evident and represent the visible alterations in these rock samples (figure 5g to h).

Essential minerals

Plagioclase is one of the essential minerals in the investigated monzogabbro-monzodiorite, making up a significant proportion of their volume. Plagioclase crystals are euhedral to subhedral and display polysynthetic twinning and compositional zoning. In some instances, they contain apatite inclusions. Additionally, plagioclase grains are partially altered to sericite, epidote, and calcite in some cases.

Pyroxene is present as scattered, isolated grains or as cores within amphiboles and micas. These pyroxenes are mostly subhedral to anhedral and primarily belong to the clinopyroxene group. The occurrence of pyroxene cores within amphiboles and micas suggests that, through the process of fractional crystallization and increasing water content, amphiboles and micas are crystallized in the late stages.

Amphiboles (green and brown hornblende) are abundant in monzogabbro-monzodiorite samples, appearing in euhedral to subhedral forms. The ubiquitous presence of amphibole and mica in these rocks suggests that the parent magma was enriched in water (1.6 to 4.3 wt.%, based on 16 whole rock geochemical analyses). As the magma cools and crystallizes, the presence of water profoundly influences the stability, nucleation, and growth of mineral products (e.g., Foden & Green, 1992; Moore & Carmichael, 1998). Therefore, concerning high-water content in the studied rocks, iron- and magnesium-rich amphiboles and micas

crystallized, rather than pyroxene or olivine.

Detailed petrographic observations and backscatter image analysis reveal that some biotites contain cores of amphibole (green or brown hornblende). This indicates that during the magmatic fractionation process, the concentration of potassium (K_2O) in the melt gradually increased. Additionally, the water content in the magmatic system also rose, creating favorable conditions for the formation of mica (biotite). Some biotites crystallized as independent minerals, while others host inclusions of zircon, apatite, and opaque minerals (magnetite, titanomagnetite and ilmenite) (see figure 5).

Accessory minerals

Apatite occurs as elongated needles, scattered grains, and inclusions within mafic minerals and plagioclase, making it one of the key accessory minerals in these rock samples. In some cases, apatite is associated just with opaque minerals. The presence of massive iron-apatite ore deposits highlights the high phosphate content in the magma that formed these rocks, explaining the abundance of apatite in the region. Representative back-scatter electron scanning (BSE) images of the pyroxenes, amphiboles, and biotite are presented in figure 6.

Opaque minerals of these rocks have occurred in both magmatic (primary) and hydrothermal (crystallized from late-stage fluids) forms. These minerals are predominantly magnetite, titanomagnetite, ilmenite, and, in some cases, specularite or hematite. They are present in the rock as dispersed, fine-grained, euhedral to subhedral, and even anhedral forms. Some of these minerals have undergone alteration, transforming into hematite and sphene. Fe and Ti-bearing minerals, such as titanomagnetite, were altered to sphene or titanite. In these cases, opaque minerals are altered into secondary sphene along their margins, cleavages, and fractures. The resulting sphene (or titanite) often appears in anhedral forms. This phenomenon indicates that Ca and Si-rich fluids have interacted with opaque minerals (see Tyler & Marsden, 1938; Mücke & Bhadra Chaudhuri, 1990). Overall, sphene ($CaTiSiO_5$) was formed during these alteration processes. Typically, the calcium and silicon required for these reactions are derived from the alteration or breakdown of plagioclase or other Ca and Si-bearing minerals. Titanomagnetites that have been partially or incompletely altered into sphene often exhibit skeletal and lamellar structure (see figures 7 & 8).

Mineral chemistry

Pyroxene

Pyroxene is one of the essential iron- and magnesium-bearing minerals in monzogabbros. Microscopic examination, along with their oblique extinction, confirms that the pyroxenes in the samples are clinopyroxenes. In general, the structural formula for pyroxenes is calculated based on six oxygen atoms and four cations. A selection of obtained of microprobe results is given in Table 2. The Q-J diagram of Morimoto (1988), which is calculated and plotted based on the formulas $Q = Ca + Mg + Fe^{2+}$ and $J = 2Na \pm R$ (R: Al, Fe^{3+}, Cr^{3+}, Sc^{3+}), the clinopyroxenes from the study area are classified within the calcium-magnesium-iron-bearing pyroxene group (figure 9a). Additionally, based on Morimoto (1988) triangular diagram with the primary endmembers of clinoenstatite (En), clinoferrosilite (Fs), and wollastonite (Wo), the studied pyroxenes fall within the diopside, salite, and augite fields (figure 9b). In the Si vs. Al diagram (Berger et al., 2005), all analyzed pyroxenes plot above the saturation line for the aluminum and silica tetrahedral site ($Si + Al = 2$), indicating that this site in the pyroxene structure is predominantly occupied by Si and Al^{+4} cations (figure 9c). By plotting the values of $Ti + Cr + Na$ against Al, the studied pyroxenes are classified within the range of pyroxenes with igneous origin (Figure 9d).

Table 2. Selected EPMA analytical data of clinopyroxenes were calculated based on 23 oxygen atoms in the structural formula

Pyroxene	NG-01.2	NG-01.2	NG-01.2	NG-01.2	ZB15-2	ZB15-2	ZB15-2	ZB15-2
SiO_2	48.78	48.67	52.44	52.76	52.66	51.40	48.83	49.59
TiO_2	2.24	2.34	0.28	0.31	0.78	0.66	2.75	2.31
Al_2O_3	7.22	7.02	2.04	1.97	1.84	3.82	7.65	4.85
FeO^T	6.51	6.98	10.85	9.93	10.30	14.17	8.09	8.58
MnO		0.04	0.58	0.27	0.16	0.50		
MgO	12.70	12.04	11.76	11.76	12.25	15.64	12.84	13.32
CaO	21.93	21.70	20.96	21.89	21.44	12.90	18.32	20.69
Na_2O	0.63	0.80	0.81	0.74	0.58	0.60	1.26	0.61
K_2O	0.05	0.10	0.01	0.24		0.12	0.35	
Cr_2O_3	0.03	0.11	0.08	0.01	0.05	0.21	0.13	0.11
Total	100.09	99.79	99.82	99.87	100.06	100.01	100.22	100.06
T spaces								
Si	1.804	1.810	1.974	1.980	1.970	1.916	1.801	1.845
Al	0.196	0.190	0.026	0.020	0.030	0.084	0.199	0.155
Fe^{3+}	0.000	0.000	0.000	0.000	0.000	0.000	0.000	0.000
Sum	2.000	2.000	2.000	2.000	2.000	2.000	2.000	2.000
M1spaces								
Al	0.119	0.118	0.064	0.067	0.051	0.084	0.134	0.058
Fe^{+3}	0.000	0.000	0.003	0.000	0.000	0.005	0.015	0.009
Ti	0.062	0.065	0.008	0.009	0.022	0.019	0.076	0.065
Cr	0.001	0.003	0.002	0.000	0.001	0.006	0.004	0.003
Mg	0.700	0.668	0.660	0.658	0.683	0.869	0.706	0.739
Fe^{2+}	0.118	0.145	0.262	0.266	0.242	0.017	0.065	0.127
Mn	0.000	0.000	0.000	0.000	0.000	0.000	0.000	0.000
Total M1	1.000	1.000	1.000	1.000	1.000	1.000	1.000	1.000
M2 spaces								
Mg	0.000	0.000	0.000	0.000	0.000	0.000	0.000	0.000
Fe^{2+}	0.083	0.071	0.076	0.046	0.081	0.420	0.169	0.132
Mn	0.000	0.001	0.019	0.009	0.005	0.016	0.000	0.000
Ca	0.869	0.865	0.845	0.880	0.860	0.515	0.724	0.825
Na	0.045	0.058	0.059	0.054	0.042	0.044	0.090	0.044
K	0.002	0.005	0.000	0.011	0.000	0.005	0.016	0.000
Total M2	1.000	1.000	1.000	1.000	0.987	1.000	1.000	1.000
En	39.5	38.1	35.4	35.4	36.5	47.2	42.0	40.4
Fs	11.4	12.5	19.3	17.2	17.5	24.8	14.9	14.6
Wo	49.1	49.4	45.3	47.4	46.0	28.0	43.1	45.0
100Mg/ ($Mg+Fe^{2+}+Fe^{3+}+Mn$)	77.7	75.4	64.7	67.3	67.6	65.5	73.9	73.5
Fe_2O_3	0.00	0.01	0.10	0.00	0.00	0.19	0.55	0.30
FeO	6.51	6.97	10.75	9.93	10.30	14.00	7.59	8.31

Amphibole

Amphibole is one of the most significant ferromagnesian minerals in the studied monzogabbro-monzodiorites. Their structural formula follows the standard amphibole formula ($AB_2C_5IVT_8O_{22}(OH)_2$) (Leake et al., 1997), based on 23 oxygens and 13 cations occupying tetrahedral and octahedral positions. Various factors, including pressure, temperature, the presence of volatiles, water content, and oxygen fugacity, influence the mineral diversity and formation of amphiboles (Anderson & Smith, 1995; Scaillet & Macdonald, 2003; Martin, 2007; Ridolfi et al., 2010; Molina et al., 2015; Mutch et al., 2016; Ridolfi, 2021). Approximately 110 points were analyzed on amphiboles from the monzogabbro-monzodiorites of the mentioned areas. Based on data analysis in table 3, the sodium content in the B position of the amphibole formula for the samples ranges from 0.05 to 0.48 BNa, while the calcium content in this position varies between 1.52 and 1.95 BCa. When plotted on the diagrams of Leake et al., 1997 and Hawthorne et al., 2012, the studied amphiboles are classified as calcic amphiboles (figure 10a)

and indicate their formation from a water-rich magma. The abundant presence of biotite, an iron and magnesium silicate minerals, in the monzogabbro-monzodiorites of northeastern Bafq, further supports this evidence. In another classification by Leake et al., 1997, based on the Si vs. $Mg/(Mg + Fe^{2+})$ diagram, these minerals plot within the hornblende-tschermakite to hornblende-ferro-tschermakite category (figure 10b). Based on the Ti content ($Ti \geq 0.5$), $Fe/(Fe+Mg) \geq 0.5$, $Ca_B \geq 1.5$, $(Na+K)_A \geq 0.5$, and Si (apfu) between 5.5-6.5 (Leake, 1997), most of the analyzed amphiboles can also be considered as kaersutite and ferrokearsutite (figure 10c).

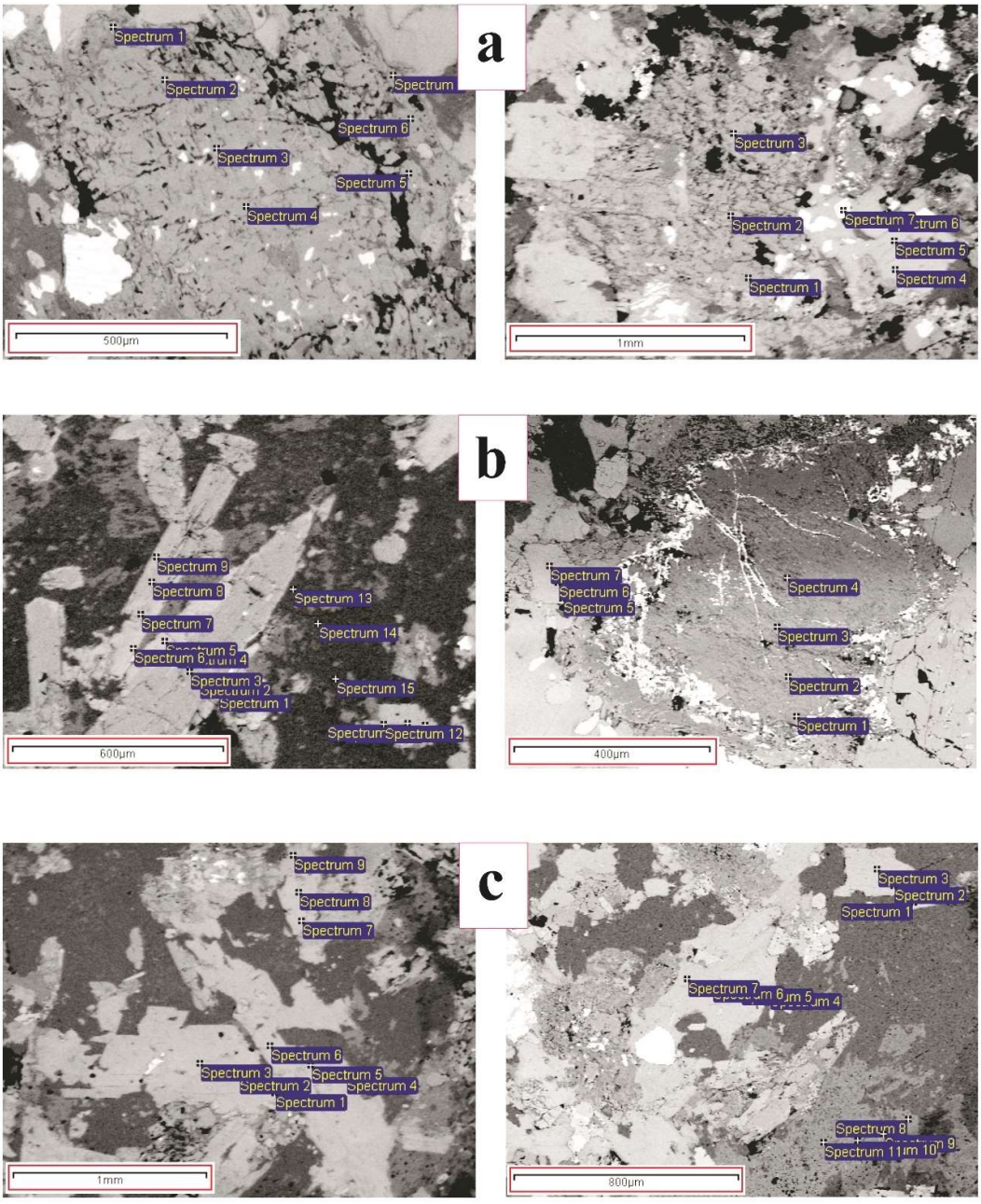

Figure 6. a) Selected BSE image of biotite with inclusions of Fe-Ti Oxides such as magnetite and ilmenite (white colour grains) from Dehnow monzogabbro. b) BSE image of amphibole, from Esfordi monzogabbro, c) BSE image of pyroxene with inclusions of Fe-Ti Oxides such as magnetite and ilmenite (white colour grains) from Dehnow monzogabbro

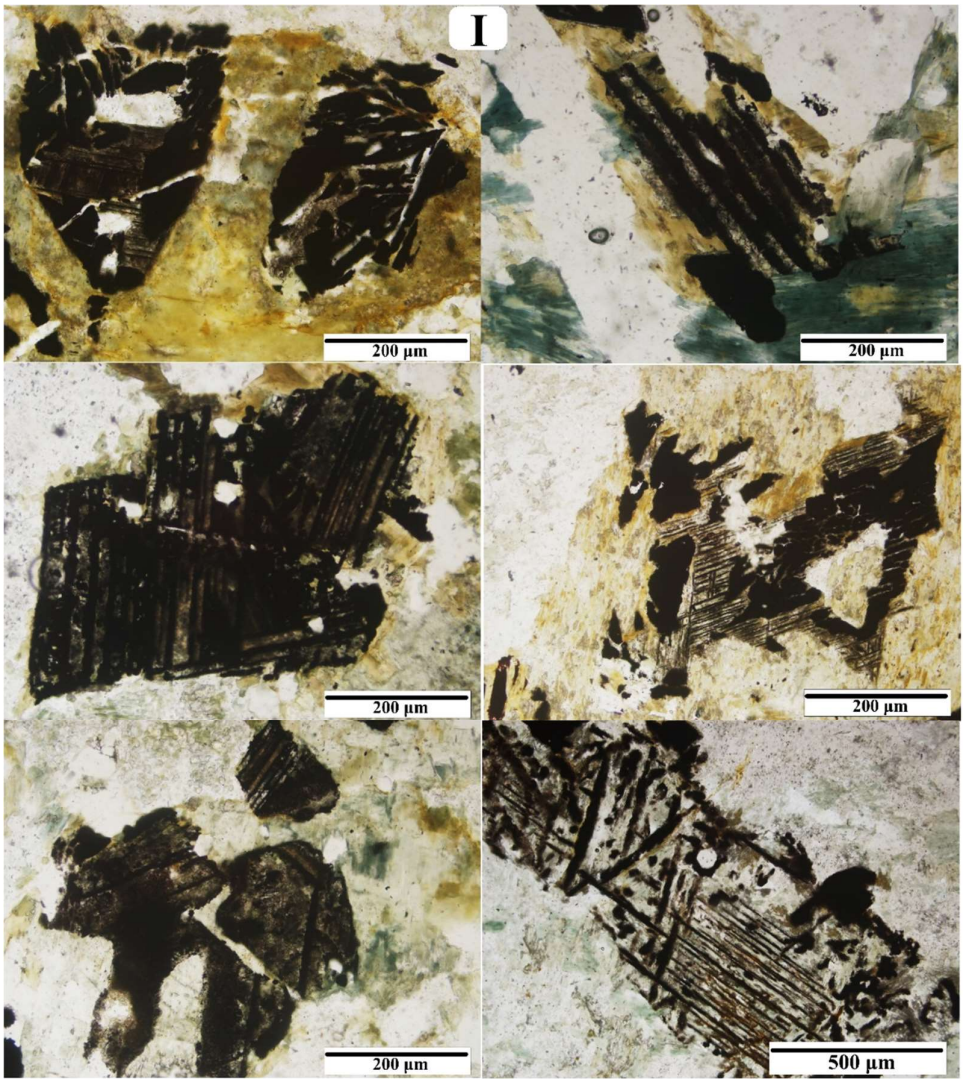

Figure 7. Photomicrographs (in PPL) of the alteration of Ti-bearing minerals to titanite or sphene. You can see some of the opaque minerals, whose isotropy features were changed. Dark, cloudy, or dusty parts are Ti-bearing minerals which altered to titanite or sphene

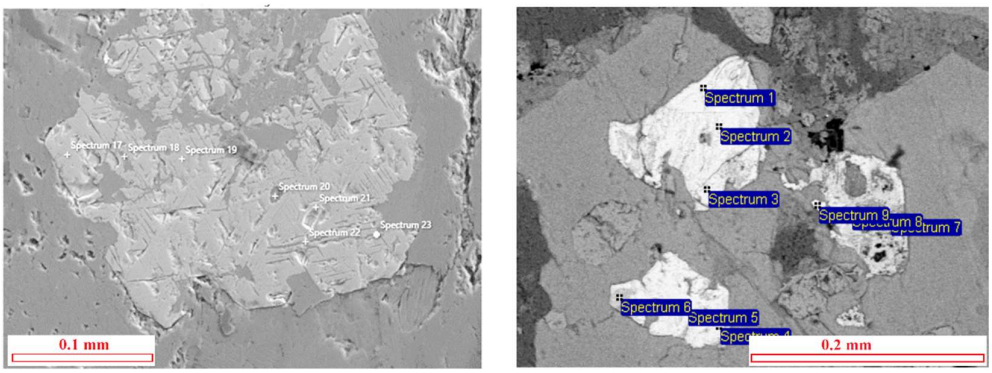

Figure 8. This is one of the BSE images from the studied monzogabbro-monzodiorites sample of the NE Bafq, showing that some of the narrow bands in magnetite are rich in Titanium, and some of them have ilmenite composition. In some of the Ti-rich zones, lamella or bands, TiO_2 contents reach to 46.32 percent, which accommodates to ilmenite composition. But, TiO_2 contents of the opaque minerals vary between 11% to 31 %

Amphibole classification based on Si atoms per formula unit (a.p.f.u.) from point analysis can help differentiate between igneous and metamorphic amphiboles. According to Agemar et al., 1999, amphiboles with Si atoms per formula unit less than 7.3 are typically of magmatic (igneous) origin, while those with Si values greater than 7.3 are likely formed through metamorphic processes. Accordingly, the amphiboles of the studied rocks have a Si range in formula units between 5.68 and 6.59, indicating that they are all in the range of amphiboles of igneous origin. Additionally, based on the Na+Ca+K vs. Si diagram (Sial et al., 1998) (figure 10d), all of the amphiboles of the studied rocks have an igneous origin. For instance, the presence of water and volatiles plays a critical role in controlling the crystallization of amphiboles.

Table 3. Selected EPMA analytical data for amphiboles were calculated based on 23 oxygen atoms in the structural formula

Amphibole	ESF-gb	ESF-gb	ESF-gb	NG-01.2	NG-01.3	NG-01.5	ZB-15.2	ZB-15.4	ZB-15.5
SiO_2	43.7	44.0	42.9	41.5	39.1	40.5	42.2	43.2	44.9
TiO_2	5.0	4.3	5.4	5.3	6.4	5.0	5.3	5.7	3.9
Al_2O_3	11.5	11.1	12.4	17.0	14.3	12.9	12.1	12.7	12.2
Cr_2O_3	0.0	0.0	0.1	0.0	0.0	0.2	0.4	0.1	0.2
Fe_2O_3	0.0	0.0	0.0	0.5	1.5	0.2	0.0	0.0	0.0
FeO	10.6	12.8	10.4	3.8	11.8	13.3	11.0	9.9	10.3
MnO	0.1	0.0	0.2	0.0	0.0	0.0	0.0	0.2	0.1
MgO	12.3	11.5	12.2	15.2	10.7	11.0	11.7	11.5	11.8
CaO	10.8	10.5	10.6	10.0	10.5	10.9	10.9	10.6	11.7
Na_2O	2.9	2.7	3.1	3.4	2.4	2.7	2.9	2.7	2.1
K_2O	1.2	1.2	1.0	1.3	1.4	1.4	1.4	1.5	0.9
H_2O*	2.1	2.0	2.1	2.1	2.0	2.0	2.0	2.1	2.1
Total	100.0	100.1	100.2	100.1	100.1	100.2	99.9	100.2	100.1
T Spaces									
Si	6.4	6.5	6.3	5.9	5.8	6.0	6.2	6.3	6.5
Al^{iv}	1.6	1.5	1.7	2.1	2.2	2.0	1.8	1.7	1.5
Sum	8.0	8.0	8.0	8.0	8.0	8.0	8.0	8.0	8.0
M1-M2 Spaces									
Al^{vi}	0.4	0.4	0.4	0.7	0.3	0.3	0.3	0.5	0.6
Ti	0.5	0.5	0.6	0.6	0.7	0.6	0.6	0.6	0.4
Fe^{3+}	0.0	0.0	0.0	0.1	0.2	0.0	0.0	0.0	0.0
Fe^{2+}	1.3	1.6	1.3	0.4	1.5	1.6	1.4	1.2	1.2
Mg	2.7	2.5	2.6	3.2	2.4	2.4	2.6	2.5	2.6
Sum	4.9	5.0	4.9	5.0	5.0	5.0	4.8	4.8	4.8
A Spaces									
Ca	1.7	1.6	1.6	1.5	1.7	1.7	1.7	1.7	1.8
Na	0.8	0.8	0.9	0.9	0.7	0.8	0.8	0.8	0.6
K	0.2	0.2	0.2	0.2	0.3	0.3	0.3	0.3	0.2
OH*	2.0	2.0	2.0	2.0	2.0	2.0	2.0	2.0	2.0
Sum	4.7	4.6	4.7	4.7	4.6	4.8	4.8	4.7	4.6
Sum cations	17.6	17.6	17.6	17.7	17.6	17.8	17.7	17.5	17.4
(Ca+Na) (B)	2.0	2.0	2.0	2.0	2.0	2.0	2.0	2.0	2.0
Na (B)	0.3	0.4	0.4	0.5	0.3	0.3	0.3	0.3	0.2
(Na+K) (A)	0.7	0.6	0.7	0.7	0.6	0.8	0.8	0.7	0.6
$Mg/(Mg+Fe^{2+})$	0.7	0.6	0.7	0.9	0.6	0.6	0.7	0.7	0.7
$Fe3/(Fe^{3+}+Al^{VI})$	0.0	0.0	0.0	0.1	0.4	0.1	0.0	0.0	0.0
Sum	12.9	13.0	12.9	13.0	13.0	13.0	12.9	12.8	12.8

The higher the water content of the magma, the more calcic the amphiboles formed, whereas lower water content leads to the formation of more sodic amphiboles (Ridolfi et al., 2010; Scaillet & Mcdonald, 2003). Since aluminum plays a fundamental role in all amphibole-forming processes, it is compared with other elements. Additionally, an increase in silicon (Si) content in the mineral correlates with a decrease in Al^{IV} (figure. 10e). In the plot of Al^{IV} versus Ti, all the studied amphiboles have Ti values below 0.8 (figure. 10f). This is because, silicon and aluminum can substitute for each other in the amphibole structure. The electric charge imbalance, which is caused by the four-coordinated Al^{IV}-substitution of Si in the tetrahedral position, may be compensated by the isomorphism replacement of Al^{IV}, Fe^{3+}, and Ti in the octahedral position (Niu et al., 2005). Also decrease in Al^{IV} is consistent with decreasing pressure.

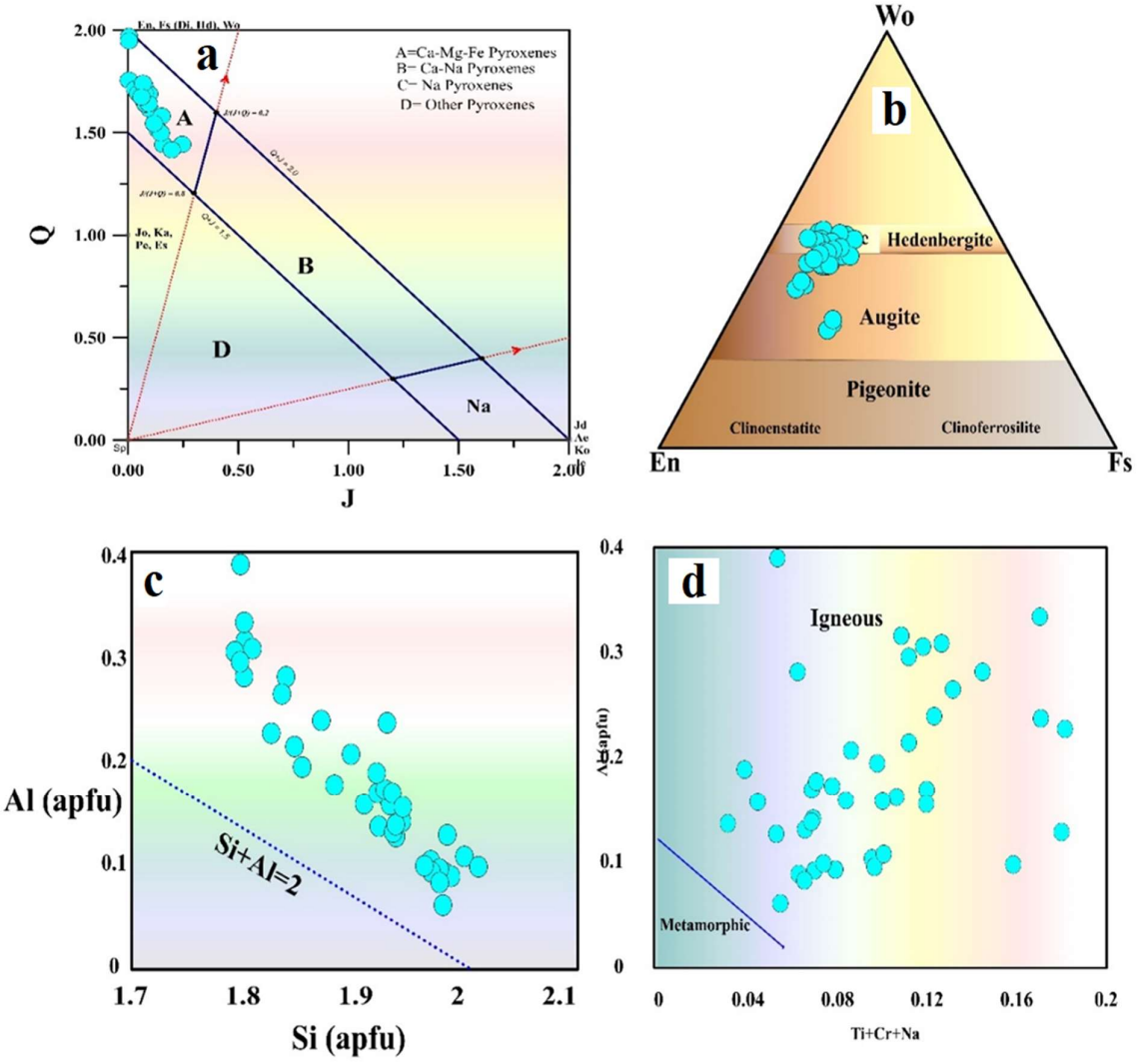

Figure 9. (a) Morimoto's Q-J diagram (1988). (b) Polderwaart and Hess' (1951) ternary diagram with three main vertices or poles of clinoenstatite (En), clinoferrosilite (Fs), and wollastonite (Wo), to distinguish the composition of pyroxenes. (c) Si vs. Al distribution diagram and determination of saturation. (d) Berger et al.'s (2005) diagram with Ti+Cr+Na vs. Al components that distinguish igneous from metamorphic pyroxenes

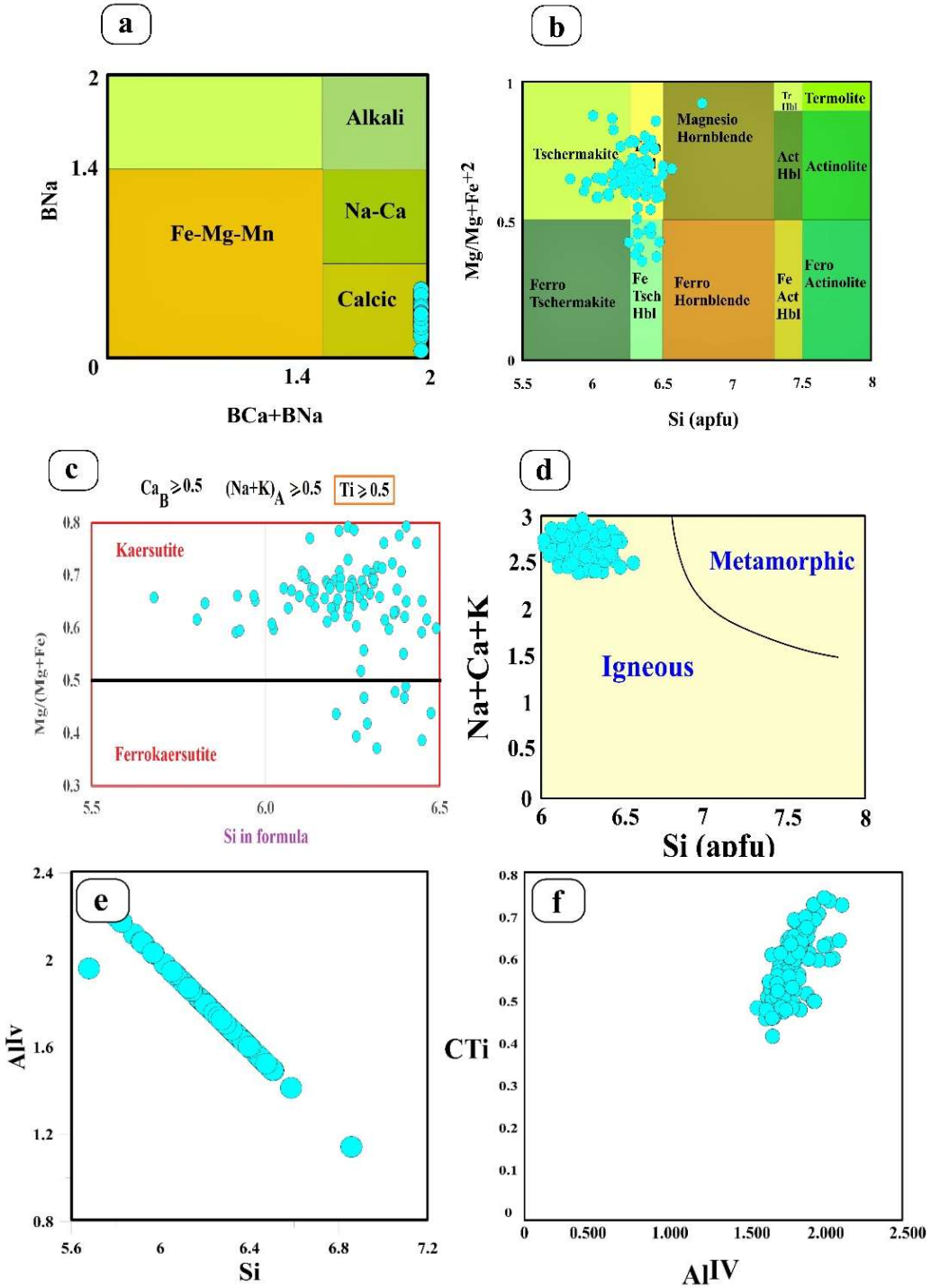

Figure 10. (a) BCa + BNa vs. BNa diagram (Leake et al., 1997), b) Si vs. Mg/(Mg + Fe^{2+}) diagram (Leake et al., 1997), c) Fe/Fe+Mg versus Si for classification of kaersutites (Leake et al., 1997), d) Na+Ca+K vs. Si diagram (Sial et al., 1998) for chemical discrimination between metamorphic and igneous amphiboles. e) Al^{IV} vs. Si diagram, and (f) Cationic Ti vs. Al^{IV} diagram

Biotite

Accordingly, based on table 4, the triangular diagram (Al^{IV}+Fe^{3+}+Ti—Mg—Fe^{2+}+Mn) presented in figure 11a (Spear, 1984) classifies the biotites of the investigated rocks as

magnesium-rich and slightly iron-bearing biotites. To distinguish primary from secondary biotites, the ternary diagram of MgO - TiO_2×10 - FeO (Nachit et al., 2005) (figure 11b) has been employed. This diagram effectively distinguishes primary (magmatic) biotites from secondary biotites, as well as primary biotites that have undergone re-equilibration. Accordingly, the biotites of the monzogabbro-monzodiorites of northeastern Bafq are within the range of primary or magmatic biotites (figure 11b). Additionally, they observed that the enrichment of iron and magnesium in biotites largely depends on the oxidation conditions (favoring magnesium enrichment) and reduction conditions (favoring iron enrichment). Lalonde and Bernard., 1993 also highlighted a relationship between the concentrations of Fe^{2+}, Ti, and Mg and the color of biotite. Biotites of the studied rocks exhibit a distinct and prominent brown color. The widespread presence of minerals such as magnetite, ilmenite, and titanite in these samples indicates high oxygen fugacity and oxidizing conditions of the magma-forming of the studied rocks.

Table 4. Selected EPMA analytical data of biotites were calculated based on 22 oxygen atoms in the structural formula

Biotite	ESF-gb	ESF-gb	ESF-gb	NG-01.2	NG-01.3	NG-01.5	ZB-15.2	ZB-15.4	ZB-15.5
SiO_2	38.83	39.10	37.16	37.90	36.31	35.79	37.52	36.83	35.89
TiO_2	4.51	4.24	5.63	6.14	5.93	7.17	7.23	8.41	8.03
Al_2O_3	13.67	14.89	14.71	13.65	14.57	14.64	13.32	14.24	14.13
FeO^T	19.31	16.54	16.55	19.39	18.71	17.79	17.77	16.83	19.09
MnO		0.12	0.21	0.02	0.16	0.20	0.23	0.24	0.10
MgO	10.82	11.47	11.31	10.64	10.74	10.45	10.34	9.96	8.65
CaO		0.06	0.01	0.03			0.02		
Na_2O	0.38	0.77	0.79	0.43	0.33	0.70	0.78	0.81	0.89
K_2O	8.61	8.49	8.13	8.44	8.57	8.04	8.57	8.32	7.99
Cr_2O_3		0.02	0.31			0.19	0.03		0.17
Total	96.14	95.68	94.82	96.63	95.33	94.97	95.81	95.64	94.95
Z spaces									
Si	5.82	5.81	5.60	5.67	5.51	5.43	5.65	5.52	5.49
Al^{IV}	2.18	2.19	2.40	2.33	2.49	2.57	2.35	2.48	2.51
Sum z	8.00	8.00	8.00	8.00	8.00	8.00	8.00	8.00	8.00
Al^{IV}	2.18	2.19	2.40	2.33	2.49	2.57	2.35	2.48	2.51
Al^{VI}	0.24	0.41	0.21	0.07	0.12	0.05	0.01	0.04	0.03
Ti	0.51	0.47	0.64	0.69	0.68	0.82	0.82	0.95	0.92
Fe^{2+}	2.42	2.05	2.08	2.43	2.38	2.26	2.24	2.11	2.44
Mn	0.00	0.01	0.03	0.00	0.02	0.03	0.03	0.03	0.01
Mg	2.42	2.54	2.54	2.37	2.43	2.37	2.32	2.23	1.97
Cr	0.00	0.00	0.04	0.00	0.00	0.02	0.00	0.00	0.02
Y	5.58	5.49	5.54	5.57	5.63	5.54	5.41	5.36	5.40
Ca	0.00	0.01	0.00	0.00	0.00	0.00	0.00	0.00	0.00
Na	0.11	0.22	0.23	0.12	0.10	0.21	0.23	0.24	0.26
K	1.65	1.61	1.56	1.61	1.66	1.56	1.65	1.59	1.56
Total	15.10	15.02	15.28	15.20	15.50	15.42	15.06	15.02	15.13
Fe/Fe+Mg	0.50	0.45	0.45	0.51	0.49	0.49	0.49	0.49	0.55
Fe+Mg	4.84	4.59	4.63	4.80	4.81	4.62	4.56	4.34	4.41
Mg/(Mg+Fe2)	0.50	0.55	0.55	0.49	0.51	0.51	0.51	0.51	0.45

Feldspars

The feldspars from the monzogabbro-monzodiorites were analyzed at a total of 84 points, with a selection of the data presented in Table 5. Selected BSE images of plagioclases are presented in figure 12 (a & b). Variation of albite contents (Ab %) of one of the plagioclase crystals along a rim-core-rim profile or section illustrated in figure 12c. There is a little variation in Albite content in this plagioclase crystal, and a general increase in Ab% towards the rims. Figure 12d illustrates the compositional position of these feldspars in the Ab-Or-An triangular diagram (Deer et al., 1992).

Table 5. Selected EPMA analytical data of feldspars were calculated based on 8 oxygen atoms in the structural formula

Feldspar	ESF-gb	ESF-gb	ESF-gb	NG-01.2	NG-01.2	NG-01.2	ZB-15.3	ZB-15.4	ZB-15.12
SiO_2	68.3	67.9	67.6	68.0	67.7	67.9	66.4	65.4	66.8
Al_2O_3	19.3	19.6	19.8	19.3	19.3	19.6	19.3	18.7	19.8
FeO	0.2	0.3	0.2	0.6	0.6	0.4		0.1	0.6
CaO	0.1	0.4	0.5	0.3	0.4	0.3	0.2	0.0	0.9
Na_2O	11.5	11.5	11.1	11.6	11.4	11.6	6.7	2.9	10.1
K_2O	0.4	0.2	0.6	0.1	0.2	0.0	7.1	12.7	1.6
Total	99.8	99.8	99.8	99.9	99.5	99.9	99.7	99.8	99.9
Si	3.0	3.0	3.0	3.0	3.0	3.0	3.0	3.0	3.0
Ti	0.0	0.0	0.0	0.0	0.0	0.0	0.0	0.0	0.0
Al	1.0	1.0	1.0	1.0	1.0	1.0	1.0	1.0	1.0
Ca	0.0	0.0	0.0	0.0	0.0	0.0	0.0	0.0	0.0
Na	1.0	1.0	0.9	1.0	1.0	1.0	0.6	0.3	0.9
K	0.0	0.0	0.0	0.0	0.0	0.0	0.4	0.7	0.1
Total	5.0	5.0	5.0	5.0	5.0	5.0	5.0	5.0	5.0
Or (K)	2.1	0.9	3.3	0.4	0.9	0.1	40.4	73.9	9.3
Ab (Na)	97.5	97.4	94.4	98.2	97.2	98.6	58.6	25.8	86.3
An (Ca+Mn+Mg)	0.4	1.7	2.2	1.5	1.9	1.3	1.0	0.2	4.5

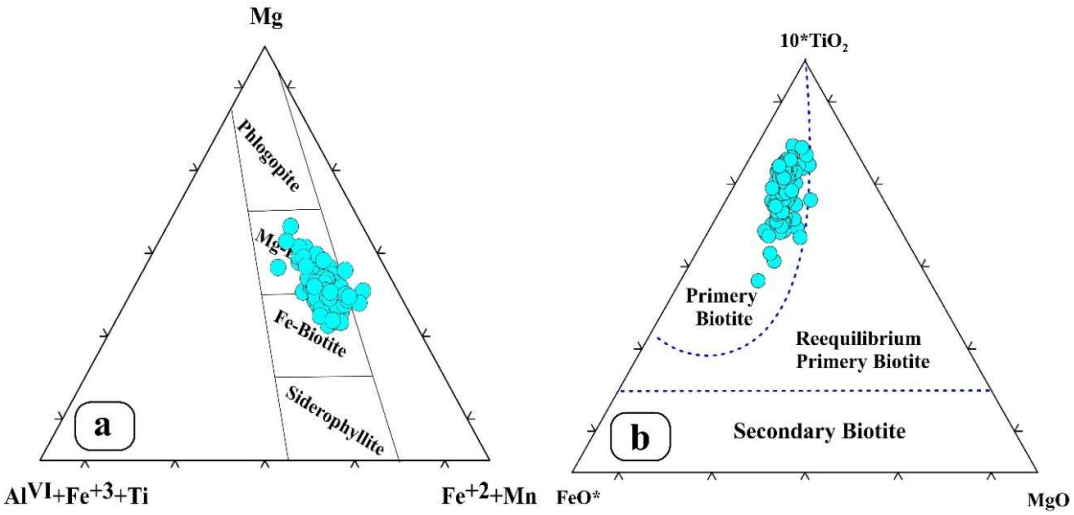

Figure 11. (a) Spear's (1984) triangular diagram to distinguish different types of biotite. (b) Nachit et al.'s (2005) triangular diagram of MgO and TiO_2*10, FeO+MnO

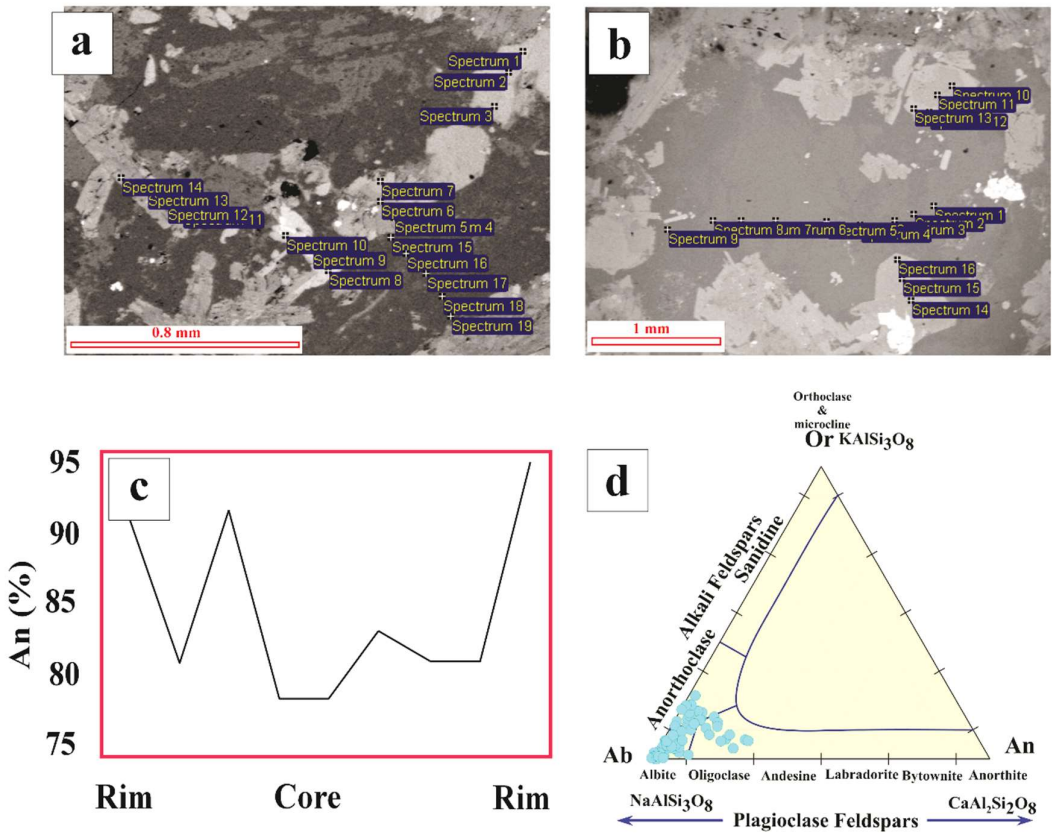

Figure 12. a and b) BSE image of plagioclase. The dark gray part of this image is plagioclase (1 to 9 points). c) Variation of Ab contents (%) in the same plagioclase that is shown in part b. d) An-Ab-Or ternary diagram for determining the composition and naming of feldspars of the monzogabbro-monzodioritic samples of the studied area (Deer et al., 1992)

The An (anorthite) content in plagioclases of basic rocks like gabbro and basalt is generally more than 50%. However, very low contents of An in the studied monzogabbro-monzodiorites is an unusual phenomenon. There are several ways to explain this subject, for example, sodic metasomatism (albitization), alteration, highly fractional crystallization, and crystallization the crystals from unusual magmas (e.g., Engvik et al., 2014; Kerwin, 2018). With attention to the geological history of the N-NE Bafq rift-related magmatic rocks, the low An content of plagioclase can be explained by metasomatism (sodic alteration (albitization)) and/or fractional crystallization of the unusual magmas (rich in Na, K, and H_2O).

Accordingly, all samples are dominated by the albite component, with some plots within the anorthoclase and oligoclase fields. Just three analyzed points have K-feldspar composition (Or_{74-88}, Ab_{9-25}, $An_{0.15-1.81}$).

Geothermobarometry

Based on the mineral chemistry of pyroxenes

The mineral chemistry of clinopyroxenes is influenced to some extent by changes in the temperature of the magma from which they crystallize. As a result, it is possible to estimate the crystallization temperature or the temperature at which chemical exchanges cease and the mineral system closes, based on the abundance or concentration of Ca, Mg, and Fe^{2+} cations in

clinopyroxenes. P-T conditions formation of the studied clinopyroxenes can be calculated using the Soesoo diagram (1997) and the following equation:

$X_{PT} = 0.446\ SiO_2 + 0.187\ TiO_2 - 0.404\ Al_2O_3 + 0.346\ FeO^{total} + 0.052\ MnO + 0.309\ MgO + 0.431\ CaO - 0.446\ Na_2O$ (Equation 1)

$Y_{PT} = -0.369\ SiO_2 + 0.535\ TiO_2 - 0.317\ Al_2O_3 + 0.323\ FeO^{total} + 0.235\ MnO - 0.516\ MgO - 0.167\ CaO - 0.153\ Na_2O$ (Equation 2)

Accordingly, the temperature formation for the studied clinopyroxenes has been estimated to range between 1139 and 1270 °C (figure. 13a & b). Pressure range mostly covers 5 to 12.33 kbars (figure. 13c & d). Also, we used from MagMin_PT spreadsheet designed by Gündüz, & Asan., 2023 for evaluating of obtained temperatures and pressures of the studied clinopyroxenes. The results are consistent with P-T ranges, which were calculated by using the Soesoo diagram (1997) (see figure. 13 b & d).

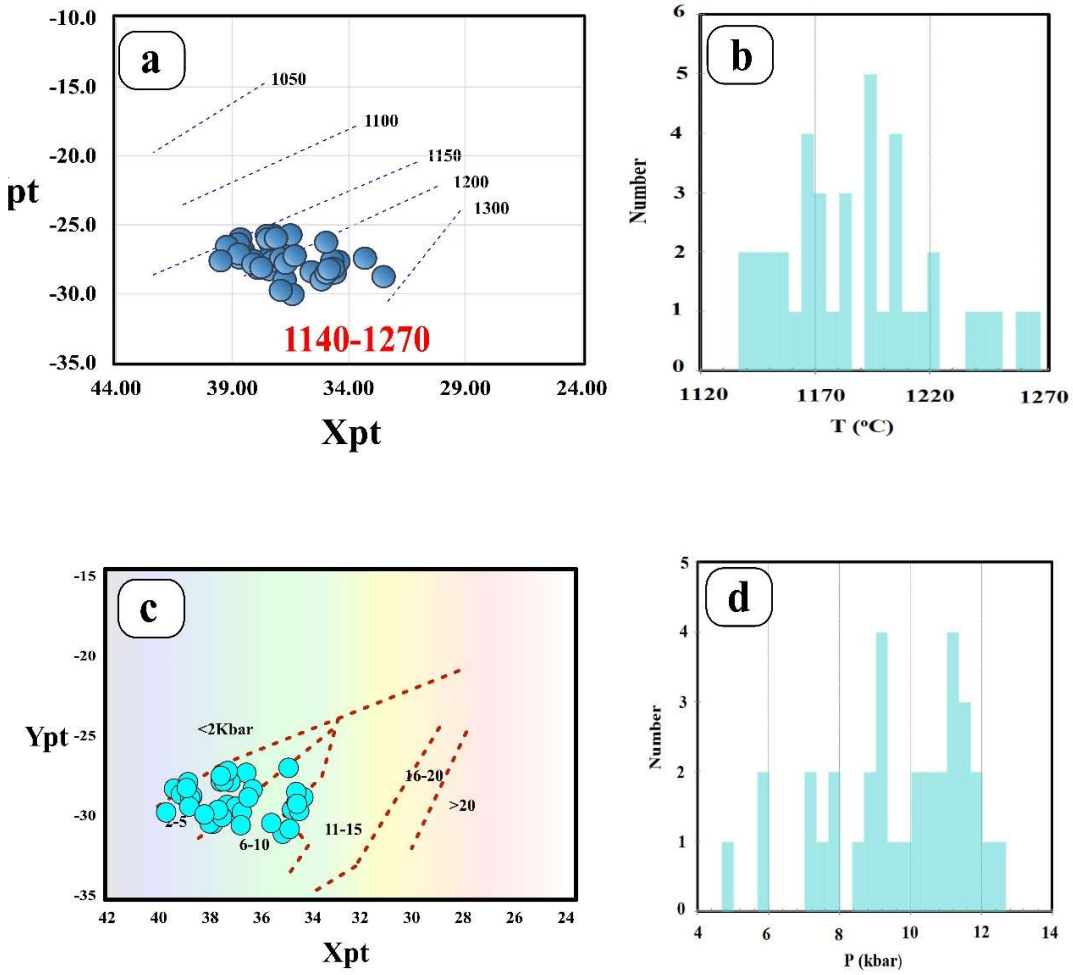

Figure 13. Geothermobarometry results based on mineral chemistry of pyroxenes. a) X_{PT} versus Y_{PT} diagrams of clinopyroxene crystallization T conditions of the N-NE monzodiorite-monzogabbros (Soesoo, 1997). b) Histogram of temperatures and pressures calculated based on clinopyroxenes thermobarometry for N-NE monzogabbro-monzodiorites based on the spreadsheet MagMin_PT designed by Gündüz & Asan (2023). c) X_{PT} versus Y_{PT} diagrams of clinopyroxene crystallization P conditions of the N-NE monzodiorite-monzogabbros (Soesoo, 1997). d) Histogram of temperatures calculated based on clinopyroxenes thermometry of the N-NE monzodiorite-monzogabbros based on the spreadsheet MagMin_PT (Gündüz & Asan, 2023)

Based on the mineral chemistry of amphiboles

Amphiboles are among the most valuable minerals for geothermobarometry of ferromagnesian minerals in calc-alkaline igneous rocks, especially in the investigated monzogabbro-monzodiorites. This is due to the widespread presence of amphibole in nearly all such rocks, regardless of whether they are basic, intermediate, or acidic in composition (Stein & Dietl, 2001; Leake et al., 1997). Amphibole remains stable across a wide range of pressures, from 23 to 1 kilobar, and temperatures, from 1150 to 400 °C, as well as in environments with water content (weight percent H_2O) exceeding 2% (Blundy & Holland, 1990). It effectively reflects the temperature, pressure, and oxygen fugacity conditions of the magmas that formed the rocks containing this mineral (Anderson & Smith, 1995). Studies and experiments conducted by researchers over the past two decades have shown that the total aluminum content in amphiboles is directly related to their crystallization depth, making it a reliable parameter for thermobarometric calculations (Simakin et al., 2012; Sarjoughian et al., 2015). As mentioned earlier, barometry depends on oxygen fugacity as well as temperature. The oxygen fugacity in a magma is influenced by the composition of its source materials and is also closely tied to the tectonic setting in which the magma forms. One approach to estimating oxygen partial pressure in intrusive rocks is to examine the composition of amphiboles, using the Al^{IV} versus Fe/(Fe+Mg) diagram. All samples plot within the region of relatively high oxygen fugacity (Anderson & Smith, 1995) (figure 14), and the abundance of magnetite and titanomagnetite in the studied monzogabbro-monzodiorites provides additional confirmation of this (figures 5 & 6).

Due to the strong relationship between the aluminum content in amphiboles and the pressure at which they crystallized; amphiboles are extensively used to estimate the pressure conditions during magma crystallization. Consequently, various barometric methods and associated formulas have been proposed by researchers to calculate pressure based on the aluminum content in amphiboles (e.g., Hammarstrom & Zen, 1986; Hollister et al., 1987; Johnson & Rutherford, 1989; Schmidth, 1992). Considering the variation in the Al^{total} content, which ranges between 2 and 2.6, and applying the Schmidth (1992) formula, the approximate pressure conditions for the formation and crystallization environment of the studied rocks were estimated to be between 9.36 and 6.51 kilobars, equivalent to depths of approximately 25.33 to 17.58 kilometers.

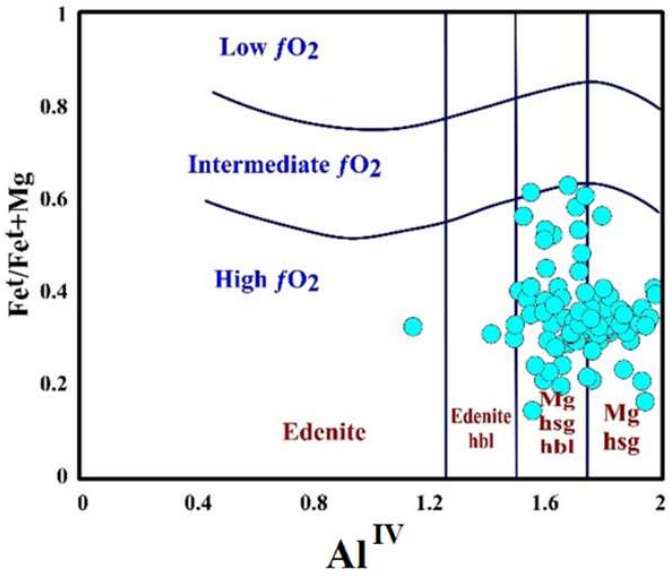

Figure 14. Determination of oxygen fugacity in the Al^{IV} vs. Fe/Fe+Mg plot (Anderson and Smith, 1995)

$$P\ (\pm\ 0.6\ kbar) = -3.01+4.76Al^{total} \quad \text{(Equation 3)}$$

The estimated pressure may be influenced by factors such as ion substitution in the amphibole structure, the fugacity of ambient oxygen, the presence of volatiles, and the chemical composition of the magma. The method of measuring pressure using the aluminum content of amphibole (barometry) is only applicable when the rock contains an assemblage of minerals, including plagioclase, potassium feldspar, biotite, amphibole, sphene, magnetite, or ilmenite. These mineral assemblages significantly constrain the chemical composition of the rock (Helmi et al., 2004), which aligns with the minerals identified in the studied monzogabbro-monzodiorites. The thermobarometric results are presented in figure 15a to e.

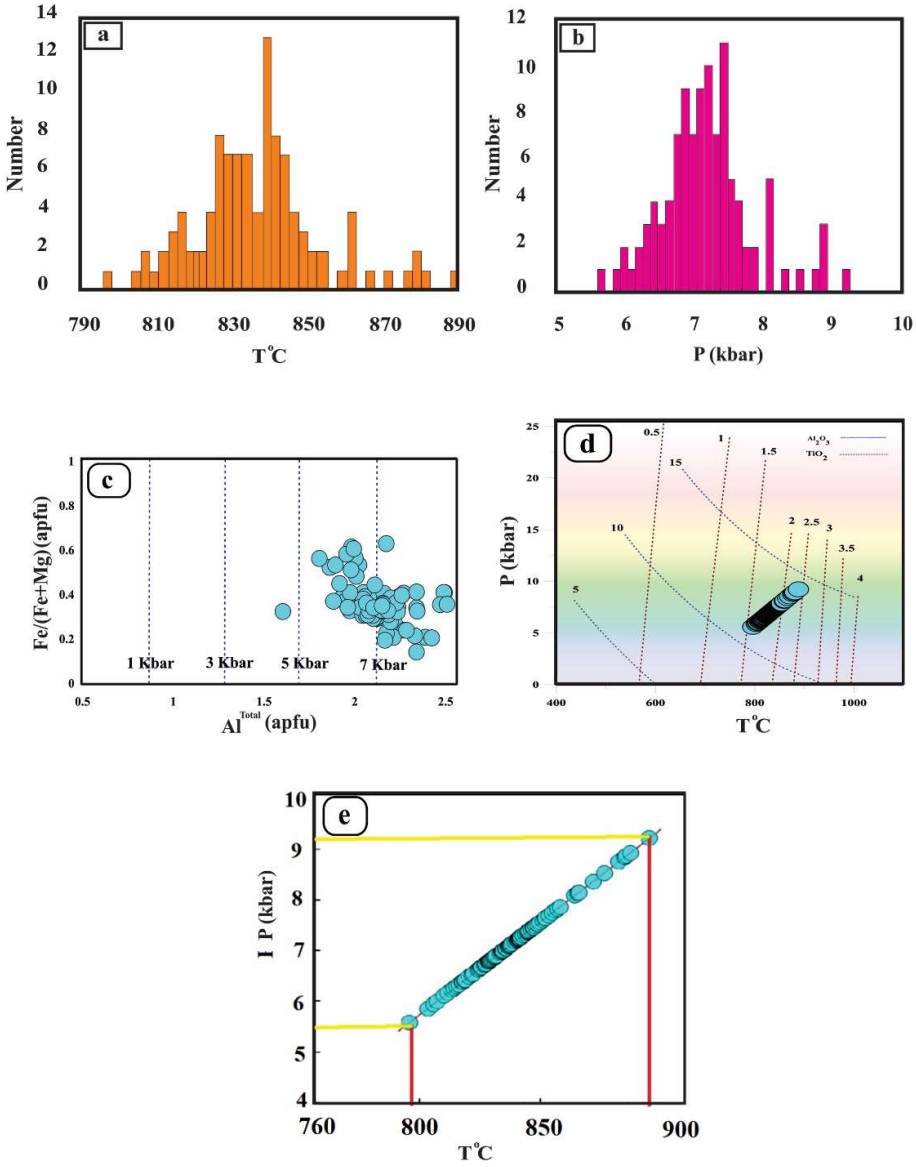

Figure 15. Geothermobarometry of amphiboles of the N-NE Bafq monzogabbro-monzodiorites. a & b) Histograms of temperatures and pressures calculated based on amphiboles geothermobarometry for N-NE monzogabbro-monzodiorites based on the spreadsheet innovated by Ridolfi (2021). c) Barometric range of amphiboles formation based on the Al^{Total} vs. Fe/Fe+Mg plot (Schmidt, 1992). d) Trend of titanium and aluminum oxide content of calcic amphiboles based on weight percent as a function of pressure and temperature (Ernst and Liu, 1998). e) P-T diagram for amphiboles of the N-NE Bafq monzogabbro-monzodiorites

The equilibrium crystallization temperature of the studied rocks, calculated using the following equation (which is referenced by Vynhal et al., 1991, to Blundy & Holland, 1990) and the pressure derived from the Schmidt formula (1992) (P (± 0.6 kbar) = -3.01+4.76Al^{total}), mainly covers a range from 790 to 890 °C.

T = (25.3 * P(kbar)) + 654.9 (Equation 4)

Also, based on the amount of different amphibole cations, temperatures of 790 to 890 °C have been obtained for the formation, cessation, and equilibrium of geochemical exchanges, based on the formula presented below:

$T\ (C^o) = 1781-132.74\ [Si^{Amph}] + 116.6\ [Ti_{Amph}] - 69.41\ [Fe^{t\ Amph}] + 101.62\ [Na^{Amph}]$ (Equation 5) (Putirka, 2016).

As amphiboles usually crystallize after pyroxene and during the increasing water content of magma, it appears that the estimated pressure range for amphiboles (5.5 to 9 kbar) is more reliable.

Based on the mineral chemistry of biotites

The titanium (Ti) content in biotites and the Ti/Fe^{2+} ratio are sensitive to temperature, making them reliable thermometers for determining the formation temperature or the equilibrium and cessation temperatures of chemical exchanges. In this regard, Henry et al., 2005 have proposed the following equation:

$T = \{[\ln(Ti)-a-c(X_{Mg})^3]/b\}^{0.333}$ (Equation 6)

where T is temperature in °C, Ti is the apfu normalized to 22 O atoms, X_{Mg} is Mg/(Mg+Fe), and the a, b, and c parameters are given in Table 6. Based on the equation "6" and using the obtained data from the microprobe analysis of biotites of the investigated monzogabbro-monzodiorites, the calculated temperatures cover mostly a range from approximately 745 to 780°C (figure. 16a, Table 6). Concerning the nature of the studied rocks, these temperatures reflect the closure temperature of the mineral system for cation exchange, rather than the crystallization temperature, as intrusive rocks undergo slow crystallization and cooling processes. Similarly, as amphiboles, where a direct relationship exists between the total aluminum content and the prevailing pressure, the total aluminum (Al^T) can also be utilized for biotite barometry, following the theory of Uchida et al., (2007). Based on the equation "7" (Uchida et al., 2007), the crystallization pressure of biotite in the rocks of the study area can be estimated. Based on equation "7", the closure pressure range for the studied biotites covers 0.3 to 2.2 kbar, but mostly falls in the range of 1.5-0.5 kbar (also see Table 7 and figure. 16 b & c).

$P(kb) = 3.03 \times Al^T - 6.53\ (\pm 0.33)$ (Equation 7) (Uchida et al., 2007)

With attention to the results of P-T calculation based on the pyroxene, amphibole, and biotite thermometry and geothermobarometry, summarized in figures 14 to 17. These results are consistent with fractional crystallisation and crystallisation order. The decreasing trend of P and T from pyroxene to biotite confirms this fact. Also, indicate P-T condition covers the following range: T= 1270 to 730 ºC, and P= 12.33 to 0.5 kbar.

Determination of magma series

Based on the mineral chemistry of pyroxenes

According to the diagram by Nisbet and Pearce, (1977), which utilizes the Al_2O_3 and SiO_2 content of pyroxenes, the magmatic series can be classified into peralkaline, subalkaline, and alkaline types. As noted by Le Bas et al., (1962), the ratio of SiO_2 to Al_2O_3 in pyroxenes is significantly and directly related to its concentration in the host rock. For this reason, due to the

high content of these two elements, particularly SiO_2, the studied pyroxenes span a broader range from subalkaline to alkaline (figure. 18a). In the diagrams by Le Bas (1962) and Le Maitre et al., (1982), where Ti is plotted against Na+Ca, most of the studied pyroxenes fall within the alkaline range (figure. 18b & c).

Table 6. Thermometry results for the studied biotites

No	Ti	X_{Mg}	T	No	Ti	X_{Mg}	T
1	0.51	0.50	769	**38**	0.69	0.49	769
2	0.52	0.46	774	**39**	0.65	0.49	771
3	0.55	0.52	766	**40**	0.68	0.50	769
4	0.47	0.55	759	**41**	0.68	0.51	768
5	0.64	0.55	760	**42**	0.82	0.51	767
6	0.67	0.52	765	**43**	0.77	0.46	774
7	0.64	0.51	767	**44**	0.77	0.58	755
8	0.59	0.51	766	**45**	0.86	0.67	730
9	0.57	0.50	768	**46**	0.71	0.47	773
10	0.55	0.59	752	**47**	0.86	0.50	769
11	0.43	0.60	749	**48**	0.81	0.50	768
12	0.49	0.58	753	**49**	0.50	0.52	766
13	0.84	0.62	745	**50**	0.82	0.53	764
14	0.40	0.62	745	**51**	0.88	0.59	751
15	0.55	0.53	764	**52**	0.93	0.65	735
16	0.56	0.54	761	**53**	1.10	0.52	766
17	0.53	0.49	769	**54**	0.97	0.51	766
18	0.62	0.50	768	**55**	0.99	0.61	746
19	0.62	0.47	773	**56**	0.65	0.42	779
20	0.56	0.48	772	**57**	0.88	0.54	762
21	0.47	0.54	763	**58**	0.38	0.51	768
22	0.52	0.50	768	**59**	0.86	0.41	780
23	0.47	0.51	766	**60**	0.59	0.49	770
24	0.52	0.53	763	**61**	0.75	0.48	772
25	0.61	0.54	762	**62**	0.82	0.54	762
26	0.60	0.53	764	**63**	0.59	0.50	768
27	0.57	0.50	768	**64**	0.67	0.46	775
28	0.49	0.53	763	**65**	0.78	0.50	768
29	0.51	0.51	767	**66**	0.67	0.50	769
30	0.50	0.52	765	**67**	0.67	0.51	767
31	0.54	0.50	768	**68**	0.80	0.57	756
32	0.54	0.67	729	**69**	0.54	0.48	771
33	0.47	0.90	616	**70**	0.56	0.48	772
34	0.43	0.91	606	**71**	0.58	0.47	772
35	0.54	0.88	632	**72**	0.53	0.51	767
36	0.41	0.94	580	**73**	0.73	0.50	769
37	0.49	0.87	640	**74**	0.65	0.51	767

Table 6. continued

No	Ti	X_{Mg}	T	No	Ti	X_{Mg}	T
75	0.69	0.49	770	**96**	0.99	0.48	772
76	0.78	0.49	770	**97**	0.85	0.49	770
77	0.70	0.49	770	**98**	0.81	0.49	770
78	0.81	0.52	765	**99**	0.94	0.45	775
79	0.69	0.52	766	**100**	0.90	0.44	776
80	0.80	0.48	772	**101**	0.74	0.40	781
81	0.83	0.49	770	**102**	0.49	0.43	777
82	0.86	0.52	765	**103**	0.39	0.48	772
83	0.93	0.46	775	**104**	0.88	0.47	772
84	0.83	0.48	771	**105**	0.83	0.47	773
85	0.82	0.48	772	**106**	0.63	0.45	776
86	0.83	0.47	773	**107**	0.71	0.55	759
87	0.91	0.46	775	**108**	0.17	0.75	701
88	0.97	0.48	772	**109**	0.06	0.77	692
89	0.82	0.51	767	**110**	0.82	0.48	772
90	0.95	0.51	766	**111**	0.96	0.51	767
91	0.92	0.45	776	**112**	0.35	0.45	776
92	0.77	0.42	779	**113**	0.91	0.42	779
93	0.85	0.44	777	**114**	0.62	0.46	774
94	0.78	0.49	770	**115**	0.53	0.42	779
95	0.92	0.41	780	**116**	0.48	0.45	775
	a	b	c				
	-2.3594	4.63E-09	-1.728				

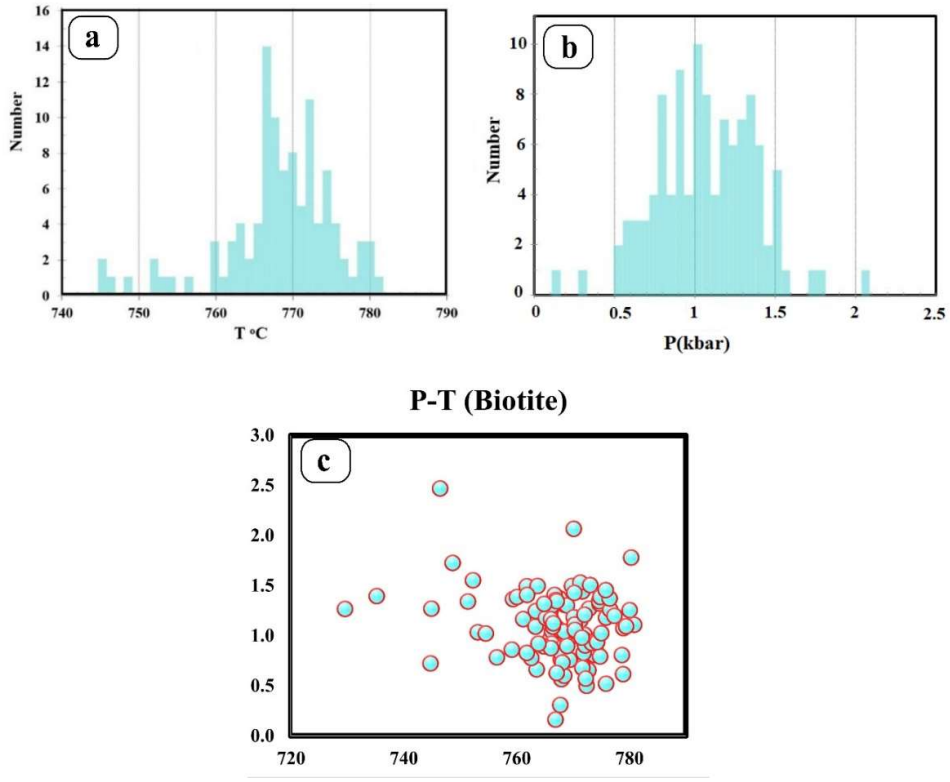

Figure 16. Thermobarometry of biotites of the N-NE Bafq monzogabbro-monzodiorites. a & b) Histograms of temperatures and pressures calculated based on biotites chemistry for N-NE monzogabbro-monzodiorites (respectively based on the Henry et al., 2005; Uchida et al., 2007); c) P-T diagram for biotites of the N-NE Bafq monzogabbro-monzodiorites

Table 7. Barometry results for the studied biotites

No	Alt	P	No	Alt	P	No	Alt	P
1	2.32	0.50	**37**	2.47	0.95	**73**	2.57	1.25
2	2.33	0.52	**38**	2.47	0.96	**74**	2.57	1.26
3	2.34	0.56	**39**	2.48	0.97	**75**	2.57	1.26
4	2.34	0.58	**40**	2.48	0.98	**76**	2.57	1.27
5	2.35	0.60	**41**	2.49	1.01	**77**	2.57	1.27
6	2.36	0.62	**42**	2.49	1.01	**78**	2.57	1.27
7	2.36	0.63	**43**	2.49	1.02	**79**	2.58	1.30
8	2.37	0.65	**44**	2.49	1.02	**80**	2.59	1.30
9	2.37	0.67	**45**	2.49	1.02	**81**	2.59	1.31
10	2.38	0.68	**46**	2.50	1.03	**82**	2.59	1.32
11	2.39	0.71	**47**	2.50	1.03	**83**	2.59	1.32
12	2.39	0.72	**48**	2.50	1.04	**84**	2.60	1.34
13	2.40	0.74	**49**	2.50	1.04	**85**	2.60	1.34
14	2.41	0.76	**50**	2.50	1.04	**86**	2.60	1.35
15	2.41	0.76	**51**	2.50	1.05	**87**	2.60	1.36
16	2.41	0.78	**52**	2.50	1.05	**88**	2.61	1.36
17	2.41	0.78	**53**	2.51	1.06	**89**	2.61	1.37
18	2.42	0.79	**54**	2.51	1.08	**90**	2.61	1.37
19	2.42	0.81	**55**	2.52	1.09	**91**	2.61	1.39
20	2.42	0.81	**56**	2.52	1.09	**92**	2.61	1.39
21	2.43	0.82	**57**	2.52	1.09	**93**	2.62	1.39
22	2.43	0.82	**58**	2.52	1.09	**94**	2.62	1.41
23	2.43	0.82	**59**	2.52	1.11	**95**	2.62	1.41
24	2.43	0.83	**60**	2.52	1.11	**96**	2.63	1.43
25	2.43	0.83	**61**	2.53	1.13	**97**	2.63	1.44
26	2.44	0.86	**62**	2.54	1.15	**98**	2.64	1.46
27	2.44	0.87	**63**	2.54	1.16	**99**	2.65	1.49
28	2.45	0.88	**64**	2.54	1.17	**100**	2.65	1.50
29	2.45	0.90	**65**	2.54	1.18	**101**	2.65	1.50
30	2.45	0.90	**66**	2.54	1.18	**102**	2.65	1.51
31	2.45	0.90	**67**	2.55	1.18	**103**	2.66	1.53
32	2.46	0.92	**68**	2.55	1.20	**104**	2.67	1.56
33	2.46	0.92	**69**	2.55	1.21	**105**	2.72	1.73
34	2.46	0.93	**70**	2.56	1.23	**106**	2.74	1.78
35	2.46	0.93	**71**	2.57	1.24	**107**	2.84	2.07
36	2.46	0.93	**72**	2.57	1.25	**108**	2.97	2.47

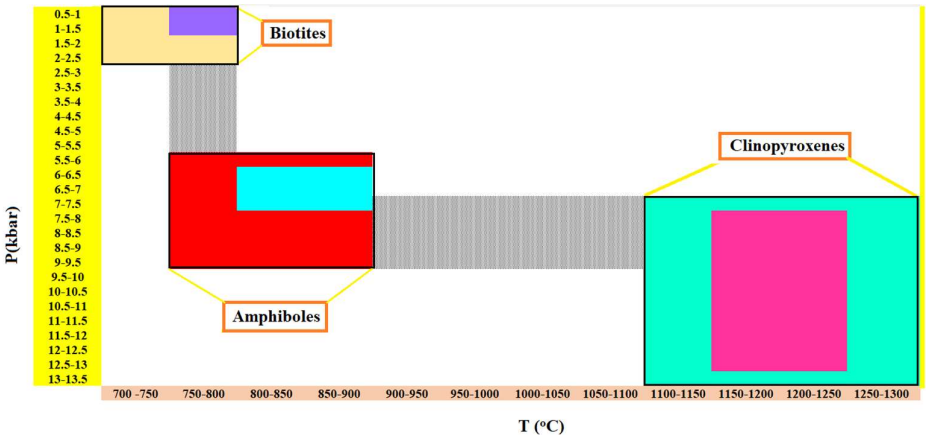

Figure 17. Total perspective of the geothermobarometry results based on the mineral chemistry of clinopyroxenes, amphiboles, and biotites of the N-NE Bafq monzogabbro-monzodiorites

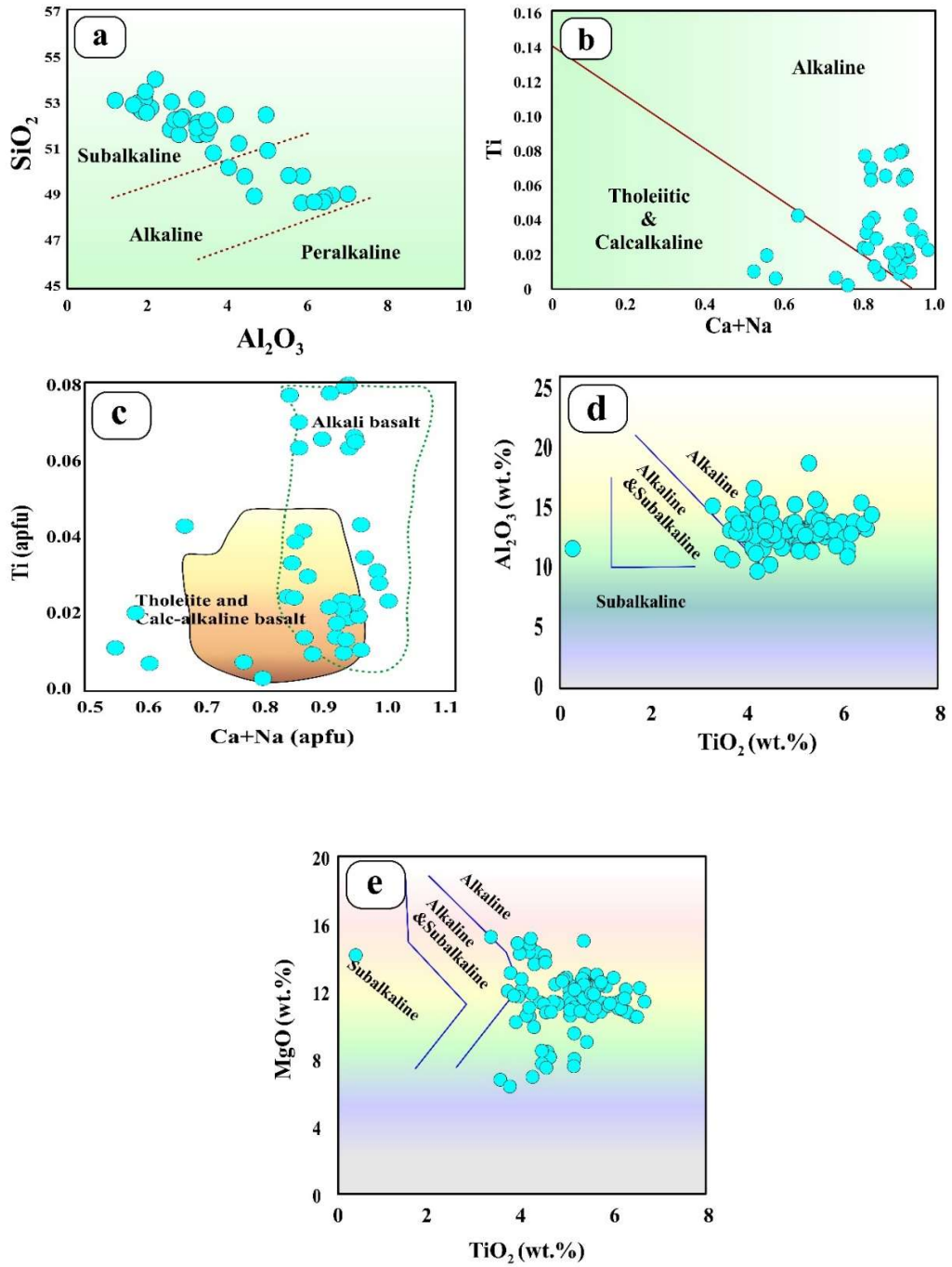

Figure 18. (a) Al_2O_3 vs. SiO_2 plot for pyroxenes (Nisbet and Pearce, 1977). (b) Ti vs. Ca + Na plot for pyroxenes (Leterrier et al., 1982). (c) Ti vs. Ca + Na plot for pyroxenes (Le Bas, 1962). (d & e) Al_2O_3 vs. TiO_2 and MgO vs. TiO_2 plots (Molina et al., 2009) to determine the magmatic series of the studied rocks, which contain amphiboles

Based on the mineral chemistry of amphiboles

By considering TiO_2 vs. Al_2O_3 and MgO vs. Al_2O_3 (Molina et al., 2009), the studied amphiboles all plot within the alkaline field (figure 18 d & e). Additionally, the presence of such amphiboles indicates that the magma forming these rocks contained a relatively significant amount of water (7.7–5.2% wt.%) (Otten, 1984).

Based on the mineral chemistry of Biotites

Based on the oxide content of major elements in biotites, such as MgO versus Al_2O_3, and FeO versus Al_2O_3 diagrams (Abdel-Rahman, 1994), can be used to determine the magmatic series and tectonic environment of rocks containing biotites. A field corresponds to the non-orogenic alkaline series, C field is associated with calc-alkaline rocks, and P field pertains to peraluminous samples resulting from the melting of continental crust in collisional environments. In these diagrams, the biotites from the monzogabbro-monzodiorites of N-NE Bafq plot within the alkaline to calc-alkaline fields (figure 19a & b).

Tectonic setting

Based on the mineral chemistry of pyroxenes

Several methods and diagrams have been developed to investigate the tectonic settings of pyroxenes. One of these diagrams is F1-F2, which that proposed by Nisbet et al., (1977). The F1 and F2 components are calculated based on the oxides of major and minor elements in pyroxenes, enabling the distinction between five different tectonic environments. Based on the formula provided for the F1 and F2 components, as outlined below, the studied pyroxenes plot in environments analogous to intraplate alkaline basalts and intraplate tholeiitic basalts (figure 20a).

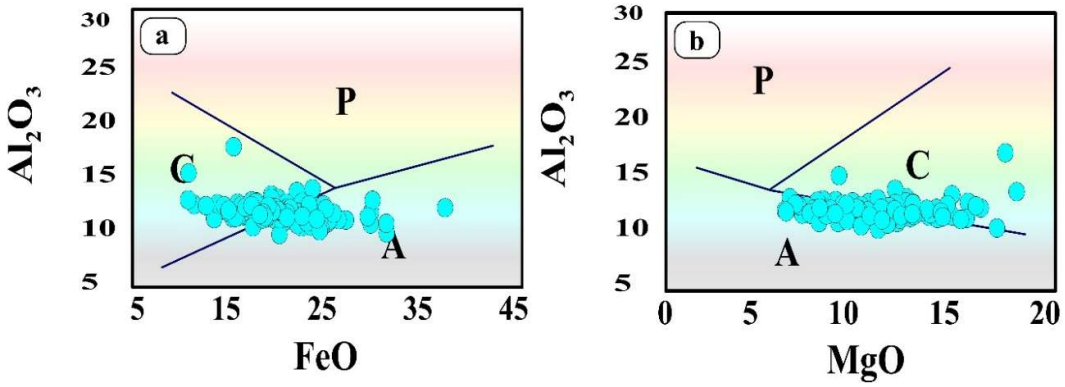

Figure 19. (a & b) FeO-Al_2O_3 and MgO-Al_2O_3 biotite discriminant diagrams (Abdel-Rahman, 1994) for the determination of the tectonic setting and magma series of the studied rocks

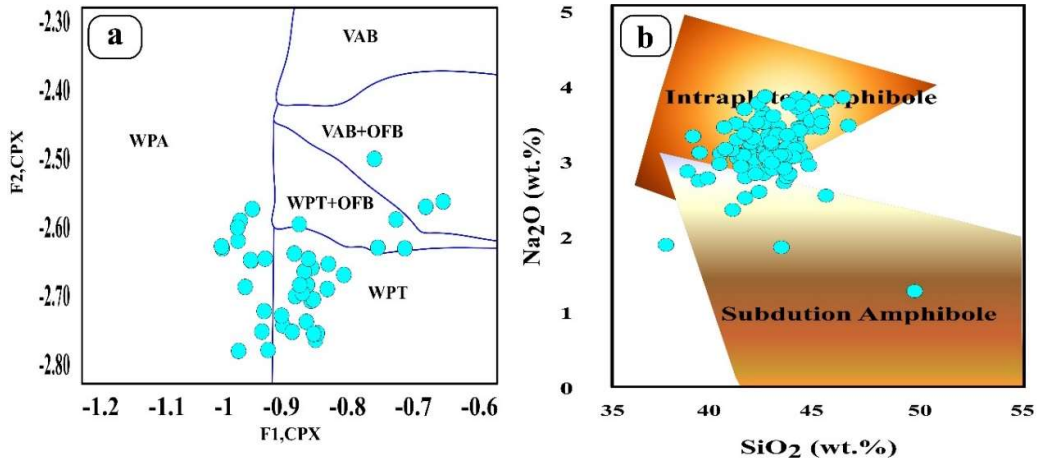

Figure 20. (a) F1-F2 diagram for pyroxenes (Nisbet et al., 1977). (b) Na_2O versus SiO_2 diagram (Coltorti et al., 2007) to distinguish the tectonic environments of the amphiboles of the studied rocks

$F1 = - (0.012*SiO_2) – (0.0807*TiO_2) + (0.0026*Al_2O_3) – (0.0012*FeO^t) – (0.0026 * MnO) +(0.0087* MgO) –(0.0128*CaO)–(0.0419*Na_2O)$. (Equation 8)

$F2 = (0.0469*SiO_2) – (0.0818*TiO_2) + (0.0212*Al_2O_3) – (0.0041*FeOt) – (0.1435*MnO) + (0.0029* MgO) – (0.0085 *CaO) – (0.016*Na_2O)$. (Equation 9)

Based on the mineral chemistry of amphiboles

One approach to determining geological settings and differentiating subduction environments from intraplate environments involves analyzing the mineral chemistry of amphiboles. Typically, amphiboles originating from intraplate environments have higher TiO_2 and Na_2O contents compared to those from subduction environments (Coltorti et al., 2007). As a result, most amphiboles of the studied rocks are indicative of formation in intraplate environments (figure. 20b).

Based on the mineral chemistry of Biotites

As discussed in the section on determining the magma series based on the chemical composition of biotites from the monzogabbro-monzodiorites of N-NE Bafq, they plot within the alkaline to calc-alkaline (as mentioned before) field or domain, consistent with rocks formed in an intracontinental rift environment (Nisbet et al.,1977; Coltorti et al., 2007; Ashrafi et al., 2024) (figure 19a & b). Additionally, the chemical composition of the pyroxenes and amphiboles in these rocks also supports an intraplate and alkaline origin.

At this moment, it is also important to note that the petrological features of the studied rocks are very similar to those of appinite rocks. Appinite rocks occur as hypabyssal intrusions and have an ultramafic to felsic composition. The hornblende in appinitic rocks is distinctly magnesian hornblende to tschermakite. Microprobe analysis and amphibole composition determinations confirm this similarity. Appinite rocks are emplaced at various crustal levels and occur in a wide range of tectonic settings. They are typically high in potassium, enriched in light rare earth elements (LRREs) and exhibit shoshonitic characteristics. Magma-forming these rocks originated from partial melting of a mantle source enriched with fluids derived from subduction zones or hydrous metasomatized mantle and subcontinental lithospheric mantle (SCLM) (Murphy, 2013). All of these criteria are consistence with the features of the N-NE Bafq basic-intermediate intrusives and/or hypabyssal dikes.

The late Neoproterozoic (late Ediacaran) - early Paleozoic (early Cambrian) magmatic rocks and their associated volcano-sedimentary rocks of central Iran, especially between Saghand, Bafq, Bahabad, and Zarand, have been the focus points of a lot of research from 1970 up to now. But until now, there are a lot of questions that should be answered for them. Those need to be more detailed studies in the future.

Conclusions

Based on the mineral chemistry results, pyroxenes have mostly diopside and augite compositions, amphiboles are calcic-amphiboles, magnesiohornblende, and tschermakite, with igneous origin. Biotites are rich in Fe and Mg, and plot in the Fe-biotite and Mg-biotite fields; they are also primary biotites. Feldspars mostly include Albite-rich or sodic plagioclase (Ab contents are more than 80 percent), and plot in albite and oligoclase fields. Concerning the presence of a variety of hydrous minerals, such as green and brown hornblende and biotite, in the monzogabbro-monzodiorite rocks, it can be concluded that these rocks crystallized from water-rich magmas. These mafic minerals frequently host opaque minerals, such as magnetite, titanomagnetite, and ilmenite, which appear as euhedral to subhedral grains and as inclusions.

Apatite, as an accessory mineral, appears as elongated needle-shaped crystals and is abundant in monzogabbros. Chemical composition of the pyroxenes, amphiboles, and biotites of the studied monzogabbro-monzodiorites supports an intraplate and alkaline to calc-alkaline origin. The main ranges of calculated temperatures for the formation, cessation, and equilibrium of geochemical exchanges of the pyroxenes, amphiboles, and biotites in respectively, are as follows:

a) 1140-1270 °C, and 4.88-12.332 kbar for pyroxenes
b) 890 to 790 °C, and 5.61-9.42 kbar for amphiboles
c) 780 to 745 °C, and 0.2-2.2 kbar for biotites (but mostly covers range of 0.5-1.5 kbar) (see figure 17).

Therefore, pressures cover a range mostly from 13.1 to 0.5 kbar, and temperatures cover a range from 1270 to 745 °C. Biotite's chemical composition is highly sensitive to environmental conditions like temperature, pressure, oxygen fugacity, and the composition of the surrounding magma and fluids. Due to this sensitivity, pressure ranges determined using biotite geobarometry should be interpreted with more caution (e.g., li & Zhang, 2022). These obtained P-T ranges, and the presence of hydrous minerals such as hornblende and biotite, are consistence with the progress of fractional crystallization during magma evolution. Based on microprobe analysis results, apatite crystals often act as a favorable host for the concentration of rare earth elements, including La, Ce, and Nd. Additionally, opaque minerals contain inclusions of monazite, a phosphate mineral rich in rare earth elements, particularly La and Ce. Collectively, these observations indicate that the studied rocks crystallized from magmas rich in water (OH), large-ion lithophile elements (LILEs) such as Sr, Ba, Rb, and K, high-field-strength elements (HFSEs) like P, Ce, La, and Zr, and light rare earth elements (LREEs) including Nd, La, and Ce (Zolala et al., 2025).

Concerning all of the new findings in this research and earlier studies, monzogabbros and monzodiorites of the N-NE Bafq belong to an extensional tectonic regime or intracontinental rifting system. Also, these rocks originated from the partial melting of metasomatized subcontinental lithospheric mantle or mantle source. The resulting magmas evolved by fractional crystallization, and possibly crustal contamination, then emplaced in the continental crust around Ediacaran-Cambrian boundary.

Acknowledgments

The authors extend their gratitude to the Vice President for research and technology at Shahrood University of Technology for the financial support provided during this study. Also, grateful to the department of geology at the Aristotle University of Thessaloniki, and the institute of geology and geophysics, Chinese academy of sciences (IGGCAS), for conducting the microprobe analysis essential to this study. We are grateful to Dr Ghasem Ghorbani and the other anonymous reviewer, who critiqued this work. Their meaningful and valuable comments or suggestions resulted in a great improvement of this paper. We would like to thank and appreciate the chief editor of the Geopersia journal, Professor Ali Kananian, technical editor Dr Elham Davtalab, Ms. Nabi Zadeh, and all of the other staff at the Geopersia Journal who kindly helped us during the acceptance of the first manuscript and the later reviewing process of this work.

Conflicts of interest

The authors declare that there are no conflicts of interest regarding the publication of this paper. No financial or personal relationships exist that could have influenced the work reported in this manuscript.

Authors' contributions

Foroogh Zolala: Conceptualization, Methodology, Software, Formal analysis, Investigation, Resources, Data Curation, Writing - Original Draft. Mahmood Sadeghian: Conceptualization, Methodology, Software, Validation, Formal analysis, Investigation, Resources, Review & Editing, Supervision, Project administration. Masood Alipour-asl: Formal analysis, Investigation, Resources, Data Curation, Review & Editing. Lambrini Papadopoulou: Formal analysis, Investigation, Resources, Data Curation, Main Funding acquisition. Zhai Mingguo: Formal analysis, Investigation, Data Curation, Funding acquisition. Foteini Aravani: Formal analysis, Data Curation, Review & Editing. Xiyan Zhu: Formal analysis, Investigation, Data Curation.

References

Abdel-Rahman, A.F.M., 1994. Nature of biotites from alkaline, calc-alkaline, and peraluminous magmas. Journal of Petrology, 35: 525-541.

Abdollahi, M., 2021. Geology, mineralogy, geochemistry, and genesis of iron mineralization in the Majerad region (southeast of Shahrood). M.Sc. Thesis, Shahrood University of Technology, Department of Earth Sciences. (In Persian with English abstract).

Agemar, T., Wörner, G., and Heumann, A., 1999. Stable isotopes and amphibole chemistry on hydrothermally altered granitoids in the North Chilean Precordillera: a limited role for meteoric water. Contributions to Mineralogy and Petrology, 136: 331-344.

Aghanabati, A., 2004. Geology of Iran. A Publication of the Geological Survey of Iran, 582 pp. (in Persian).

Aghanabati, A., Haghi-Pour, A., 2002. Geological map of Tabas (Scale 1:250,000). Geological Survey of Iran, Tehran. (In Persian).

Aghanabati, A., Saeedi, A., 2011. Geological map of Abdoughi (Scale 1:250,000). Geological Survey of Iran, Tehran. (In Persian).

Ahmadi-Moghadam, P., 2019. Petrogenesis of Mafic Igneous Rocks in the Hormoz Series, Southern Iran. Ph.D. Thesis, Hormozgan University, Faculty of Earth Sciences, Department of Petrology, 333 p. (in Persian with English abstract).

Amini, B., Rashidi, H., Poshtkuhi, M., Keshani, F., 2004. Geological map of Bafq (Scale 1:100,000). Geological Survey of Iran, Tehran. (In Persian).

Anderson, J.L., Smith, D.R., 1995. The effects of temperature and fO_2 on the Al in-hornblende barometer. American Mineralogist, 80: 549-559. https://doi.org/10.2138/am-1995-5-614

Asadi-Sarshar, M., Shafaii-Moghadam, H., Griffin, W.L., Santos, J.F., Stern, R.J., Ottley, C.J., Sarkarinejad, Kh., Sepidbar, F., O'Reilly, S.Y., 2020. Geochronology and geochemistry of exotic blocks of Cadomian crust from the salt diapirs of SE Zagros: the Chah-Banu example. International Geology Review, DOI:10.1080/00206814.2020.1787236

Ashrafi, N., Dabiri, R., Jahangiri, A., 2024. Some chemical variations in biotite, phlogopite, and muscovite, considering their tectonic setting. Geopersia, 14(2): 307-325. DOI: 10.22059/GEOPE .2024.373882.648749

Aydin, F., Karsli, O., and Sadiklar, M.B., 2009. Compositional Variations, Zoning Types and Petrogenetic Implications of Low-pressure Clinopyroxenes in the Neogene Alkaline Volcanic Rocks of Northeastern Turkey. Turkish Journal of Earth Sciences (Turkish J. Earth Sci.), 18: 163-186.

Azhdari, A., Nazari, H., Aghanabati, A., 2003. Geological map of Robat-e-khan (Scale 1:100,000). Geological Survey of Iran, Tehran. (In Persian).

Berger, J., Femenias, O., Mercier, J., and Demaiffe, D., 2005. Ocean-floor hydrothermal metamorphism in the Limousin ophiolites (western French Massif Central): evidence of a rare preserved Variscan oceanic marker. journal of Metamorphic geology, 23: 795-812.

Blundy, J.D., Holland, T.J.B., 1990. Calcic amphibole equilibria and a new amphibole plagioclase geothermometer. Contribution to Mineralogy and Petrology, 104: 208-224.

Bonyadi, Z., 2011. Mineralization and alteration in Se-Chahun Fe deposit, Bafq, Yazd Province. Ph.D. Thesis, Tarbiat Moalem University of Tehran, Faculty of Sciences, 179 p. (in Persian with English

abstract).
Bonyadi, Z., Sadeghi, R., 2019. Hydrothermal alteration associated with magnetite mineralization in the Bafq Iron deposits, Iran. Journal of Asian Earth Sciences. https://doi.org/10.1016/j.jseaes. 2019.104152.
Coltorti, M., Bonadiman, C., Faccini, B., Grégoire, M., O'Reilly, S. Y., Powell, W., 2007. Amphiboles from suprasubduction and intraplate lithospheric mantle. Lithos, 99: 68-84.
Deer, W.A., Howie, R.A., Zussman, J., 1992. An introduction to the rock-forming minerals. Second Editions, Longman, London, 696p.
Djokovic, I., Dimitrijevi, M.N., Cukucan, M., (1972). Geological map of Baghin (Scale 1:100,000). Geological Survey of Iran, Tehran. (In Persian).
Engvik, A.K., Ihlen, P.M. and Austrheim, H., 2014. Characterisation of Na-metasomatism in the Sveconorwegian Bamble sector of south Norway. Geoscience Frontiers, 5(5): 659-672.
Ernest, W.G., Liu, J., 1998. Experimental phase-equilibrium study of Al- and Ti-contents of calcic amphibole in MORB-A semiquantitative thermobarometer. American Mineralogist, 83: 952-969.
Ernst, W.G., 2002. Paragenesis and thermobarometry of Ca-amphiboles in the Barcroft granodioritic pluton, central White Mountains, eastern California. American Mineralogist, 87: 478-490.
Faramarzi, N.S., Jamshidibadr, M., Heuss-Assbichler, S., Borg, G., 2019. Mineral chemistry and fluid inclusion composition as petrogenetic tracers of iron oxide-apatite ores from Hormuz Island, Iran. Journal of African Earth Science, 155: 90-108. https://doi.org/10.1016/j.jafrearsci.2019.03.018
Foden, D., Green, D.H., 1992. Possible role of amphibole in the origin of andesite: some experimental and natural evidence. Contributions to Mineralogy and Petrology 109: 479-493.
Ghaemi, F., Saeedi, A., 2006. Geological map of Chadormalou (Scale 1:100,000). Geological Survey of Iran, Tehran. (In Persian).
Griffis, R., Kluyver, H.M., Alavi-Naini, M., 1981. Geological map of Nayband (Scale 1:250,000). Geological Survey of Iran, Tehran. (In Persian).
Griffis, R., Kluyver, H.M., Alavi-Naini, M., Chance, P.N., Meixner, H.M., Tirrul, R., 1959. Geological map of Nayband (Scale 1:100,000). Geological Survey of Iran, Tehran. (In Persian).
Gündüz, M. and Asan, K., 2023. MagMin_PT: An Excel-based mineral classification and geothermobarometry program for magmatic rocks. Mineralogical Magazine, 87(1): 1-9.
Hafezian, G., Jamali, H., 2015. Geochemistry and genesis of magnetite-apatite mineralization in Gazestan, east of Bafq . Journal of Petrology, 6(24): 39-64 (In Persian).
Haghi-pour, A., Pelissier, G., Bolurchi, M.H., Valeh, N., Aghanabati, A., Davoudzadeh, M., Stocklin, J., Sluiter, W., Natn, G., 1972. Geological map of Ardakan (Scale 1:250,000). Geological Survey of Iran, Tehran. (In Persian).
Hammarstrom, J.M., Zen, E., 1986. Aluminum-in-hornblende: an empirical igneous geobarometer. American Mineralogist, 1297-1313.
Hassanzadeh, J., Stockli, D.F., Horton, B.K., Axen, G., 2008. U-Pb zircon geochronology of the late Neoproterozoic–early Cambrian granitoids in Iran: Implications for paleogeography, magmatism, and exhumation history of Iranian basement. Tectonophysics, 451: 71-96.
Hawthorne, F.C., 1983. Crystal chemistry of the amphiboles. Canadian Mineralogist, 21: 174-481.
Hawthorne, F.C., Oberti, R., Harlow, G.E., Maresch, W.V., Martin, R.F., Schumacher, J., Welch, M., 2012. Nomenclature of the amphibole supergroup. American Mineralogist, 97: 2031-2048.
Heidari, Z., 1996. Study of volcanism in the Esfordi and Zarigan regions. M.Sc. Thesis, Shahid Beheshti University of Tehran, Faculty of Sciences, 135 p. (in Persian).
Helmy, H.M., Ahmed, A.F., El Mahallawi, M.M., Ali, S.M., 2004. Pressure, temperature and oxygen fugacity conditions of calc-alkaline granitoids, Eastern Desert of Egypt, and tectonic implications. Journal of African Earth Sciences, 38: 255-268.
Henry, D.J., Guidotti, C.V., Thomson, J.A., 2005. The Ti-saturation surface for low-to-medium pressure metapelitic biotites: Implications for geothermometry and Ti-substitution mechanisms. American Mineralogist, 90(2-3): 316-328.
Hollister, L.S., Grissom, G.C., Peters, E.K., Stowell, H.H., Sisson, V.B., 1987. Confirmation of the empirical correlation of Al in hornblende with pressure of solidification of calc-alkaline plutons. American Mineralogist, 72: 231-239.
Hossain, I., Tsunogae, T., Jannatun, N., Rahman, M. S., Nahar, M., Hasan, A. M., Khatun, M. M., 2023. Mineral compositional constraints on the petrogenesis of gabbroic and monzodioritic rocks in

Rangpur District, NW Bangladesh. Journal of Asian Earth Sciences, doi.org/10.1016/j.jaesx.2022.100134

Huckriede, R., Kursten, M., & Venzlaff, H., 1962. Zur geologie des gebietes zwischen Kerman and Sagand (Iran). Beihefet Zum Geologisschen Jahrbuch. 51: 197 p.

Ishihara, S., 1977. The magnetite series and ilmenite-series granitic rocks. Mining Geology, 27: 293-305.

Johnson, M.C., Rutherford, M.J., 1988. Experimental calibration of an Aluminum-in-hornblende geobarometer applicable to calc-alkaline rocks. EOS, Transactions American Geophysical Union 69: 1511.

Kerwin, S.P., 2018. Sodic alteration in magmatic-hydrothermal systems. Northern Illinois University.

Kluyver, H.M., Griffis, R., Alavi Naeini, M., 1981. Geological map of Nayband (Scale 1:250,000). Geological Survey of Iran, Tehran. (In Persian).

Kluyver, H.M., Griffis, R., Chance, P.N., Meixner, H.M., Tirrul, R., 1959. Geological map of Nayband (Scale 1:100,000). Geological Survey of Iran, Tehran (In Persian).

Lalonde, A.E., Bernard, P., 1993. Composition and color of biotite from granites; two useful properties in characterization of plutonic suites from the Hepburn internal zone of Wopmay Orogen, Northwest Territories. The Canadian Mineralogist, 31: 203-217. DOI: 10.2113/gscanmin.41.6.1381

Le Bas, M.J., 1962. The role of aluminum in igneous clinopyroxenes with relation to their parentage. American Journal of Science, 260: 267-288. https://doi.org/10.2475/ajs.260.4.267

Le Bas, M.J., Le Maitre, R.W., Streckeisen, A., Zanettin, B., 1986. A chemical classification of volcanic rocks based on the total alkali-silica diagram. Journal of Petrology, 27: 745-750.
https://doi.org/10.1093/petrology/27.3.745

Leake, B.E., Woolley, A.R., Arps, C.E.S., Birch, W.D., Gilbert, M.C., Grice, J.D., Hawthorne, F.C., Kato, A., Kisch, H.J., Krivovochev, V.G., Linthout, K., Laird, J., Mandarino, J.A., Maresch, W.V., Nickel, E.H., Rock, N.M.S., Schumacher, J.C., Smith, D.C., Stephenson, N.C.N., Ungaretti, L., Whittaker, E.J.W., Youzhi, G., 1997. Nomenclature of amphiboles: report of the subcommittee on amphiboles of the International Mineralogical Association, Commission on New Minerals and Mineral Names. American Mineralogist, 82: 1019-1037.

Leterrier, J., Maury, R. C., Thonon, P., Girard, D., Marchal, M., 1982. Clinopyroxene composition as a method of identification of the magmatic affinities of paleo-volcanic series. Earth and Planetary Science Letters, 59: 139-154.

Li, X., Zhang, C., 2022. Machine learning thermobarometry for biotite-bearing magmas. Journal of Geophysical Research: Solid Earth, 127(9), DOI: 10.1029/2022JB024137

Lotfi, M., Hariri, A., and Farkhondi, F., 1998. An Attitude on iron mineralization in the Gelmandeh area (northeast of Saghand). Second Conference of the Geological Society of Iran (In Persian).

Mahdavi, M.A., Aghanabati, A., Soheili, M., Mohajjel, M, Hukriede, R., Haj-Mola-Ali, A., 1996. Geological map of Ravar (Scale 1:250,000). Geological Survey of Iran, Tehran. (In Persian).

Majidi, A., Babakhani, A.R. (2000) Geological map of Ariz (Scale 1:100,000). Geological Survey of Iran, Tehran. (In Persian).

Majidi, S.A., Omrani, J., Troll, V.R. et al., 2021. Employing geochemistry and geochronology to unravel genesis and tectonic setting of iron oxide-apatite deposits of the Bafq-Saghand metallogenic belt, Central Iran. International Journal of Earth Sciences (Geol Rundsch) 110: 127-164.

Martin, R.F., 2007. Amphiboles in the igneous environment. Reviews in Mineralogy and Geochemistry, 67(1): 323-358.

Masoudi, F., Mohajjel, M., Shaker-Ardekani, F., 2008. Investigation of chemical and structural changes and determination of temperature in a progressive deformation: Evidence from the Zarrin shear zone, Ardakan. International Journal of Geoscience, 73: 11-16.

Mehdipour Ghazi, J., Moazzen, M., Rahgoshay, M., Wilde, S.A., 2021. Zircon U–Pb–Hf isotopes and whole rock geochemistry of magmatic rocks from the Posht-e-Badam Block: A key to tectonomagmatic evolution of Central Iran. Gondwana Research, 87: 162-187.

Mokhtari, A.A., 2015. Posht-e-Badam Metallogenic Block (Central Iran): A suitable zone for REE mineralization. Central European Geology, 58 (3): 199-216.

Mokhtari, M. A., Ebrahimi, M., Javidfar, B., Nabavi Sheghaghi, S.T., 2016. Petrology and Geochemistry of syenitic and gabbroic intrusive rocks in the north of Esfordi Phosphate mine (NE Bafq). Researches in Earth Sciences, 7(4): 1-21.

Molina, J.F., Scarrow, J.H., Montero, P.G., Bea, F., 2009. High-Ti amphibole as a petrogenetic indicator of magma chemistry: evidence for mildly alkalic-hybrid melts during evolution of Variscan basic–ultrabasic magmatism of Central Iberia. Contributions to Mineralogy and Petrology, 158: 69-98.

Molina, J.F., Moreno, J.A., Castro, A., Rodríguez, C. and Fershtater, G.B., 2015. Calcic amphibole thermobarometry in metamorphic and igneous rocks: New calibrations based on plagioclase/amphibole Al-Si partitioning and amphibole/liquid Mg partitioning. Lithos, 232: 286-305.

Morimoto, N., 1988. Nomenclature of pyroxenes. Mineralogy and Petrology, 39: 55-76.

Moore, G., Carmichael, I.S.E., 1998. The hydrous phase equilibria (to 3 kbar) of an andesite and basaltic andesite from western Mexico: constraints on water content and conditions of phenocryst growth. Contributions to Mineralogy and Petrology, 130: 304-319.

Mücke, A. and Chaudhuri, J.B., 1991. The continuous alteration of ilmenite through pseudorutile to leucoxene. Ore geology reviews, 6(1): 25-44.

Mutch, E.J.F., Blundy, J.D., Tattitch, B.C., Cooper, F.J. and Brooker, R.A., 2016. An experimental study of amphibole stability in low-pressure granitic magmas and a revised Al-in-hornblende geobarometer. Contributions to Mineralogy and Petrology, 171: 1-27.

Murphy J.B., 2019. Appinite suites and their genetic relationship with coeval voluminous granitoid batholiths. International Geology Review, DOI: 10.1080/00206814.2019.1630859

Nabavi, M.H., Iwao, Sh., Tatevosian, Sh., Valeh, N., Haghi-pour, A., Pelissier, G., Bolurchi, M., 1996. Geological map of Yazd (Scale 1: 25,0000). Geological Survey of Iran, Tehran. (In Persian).

Nachit, H., Ibhi, A., Abia, E.H., Ohoud, M.B., 2005. Discrimination between primary magmatic biotites, reequilibrated biotites, and neoformed biotites. Geomaterials (Mineralogy), Geoscience, 337: 1415-1420.

Nisbet, E.G., Pearce, J. A., 1977. Clinopyroxene composition in mafic lavas from different tectonic settings. Contributions to mineralogy and petrology, 63: 149-163.

Niu, L. F., & Zhang, H. F. (2005). Mineralogy and petrogenesis of amphiboles from intermediate-mafic intrusions in southern Taihang Mountains (in Chinese with English abstract). Geotectonica Et Metallogenia, 29(2): 269-277.

Nogol-Sadat, M. A. A., 2012. Geological map of Herisk (Scale 1:25,000). Geological Survey of Iran, Tehran.

Otten, M.T., 1984. The origin of brown hornblende in the Artfjället gabbro and dolerites. Contributions to Mineralogy and Petrology, 86: 189-199.

Parvaresh-Darbandi, M., Malekzadeh-Shafaroudi, A., Azim Zadeh, A.M., Karimpour, M.H., 2020. Magnetite mineralization properties of Narm iron mine with respect to petrology and geochemistry of its adjacent gabbroic-dioritic rocks (North of Tabas, South Khorasan Province). Journal of Petrology, 41:103-128.

Pilgrim, G.E., 1908. The geology of the Persian Gulf and the adjoining portion of Persia and Arabia. Memoirs of the Geological Survey of India, 34: 1–177.

Pirooj, H., Tahmasebi, Z., Ahmadi Khalaji, A., 2019. Mineralogy, geochemistry and radiometric dating of igneous rocks of Champeh salt dome, north Bandar-Lengeh. International Iranian Journal of Crystallography and Mineralogy, 27: DOI: 909-924. 10.29252/ijcm.27.4.909

Poshtkoohi, M., Ahmad, T. and Choudhary, A.K., 2018. Geochemistry and petrogenesis of Biabanak-Bafq mafic magmatism: Implications for the evolution of central Iranian terrane. Journal of Earth System Science, 127: 1-30. DOI: 10.1007/s12040-018-0969-5

Putirka, K.D., 2008. Thermometers and barometers for volcanic systems. Reviews in Mineralogy and Geochemistry, 69, 61–120. https://doi.org/10.2138/rmg.2008.69.3

Putirka, K.D., 2016. Amphibole thermometers and barometers for igneous systems and some implications for eruption mechanisms of felsic magmas at arc volcanoes. American Mineralogist, 101, 841–858. DOI: 10.2138/am-2016-5506

Ramezani, J., Tucker, R.D., 2003. The Saghand region, Central Iran: U–Pb geochronology, petrogenesis and implications for Gondwana tectonics. American Journal of Science, 303: 622-665. DOI: 10.2475/ajs.303.7.622

Rezaei, M., 2020. Petrology, geochemistry, isotope geology, and geodynamic model of the Do-Chah metamorphic-igneous complex (SE Shahrood). Ph.D. Thesis, Shahrood University of Technology, Department of Petrology, 279 p. (in Persian with English abstract).

Ridolfi, F., Renzulli, A., Puerini, M., 2010. Stability and chemical equilibrium of amphibole in calc-alkaline magmas: an overview, new thermobarometric formulations and application to subduction-related volcanoes. Contributions to Mineralogy and Petrology, 163: 45-66.

Ridolfi, F., 2021. Amp-TB2: An updated model for Calcic amphibole thermobarometry. Minerals, 11, 324. https://doi.org/10.3390/min11030324.

Ridolfi, F.; Zanetti, A.; Renzulli, A.; Perugini, D., Holtz, F.; Oberti, R. AMFORM, 2018. a new mass-based model for the calculation of the unit formula of amphiboles from Electron Micro-Probe analyses. Am. Mineral., 103: 1112-1125.

Sabzehei, M., 2017. Geological map of Ali Abad (Scale 1:25,000). Geological Survey of Iran, Tehran.

Sadeghian, M., Hosseini, S. H., Hemmati, A., and Shekari, S., 2017. Petrology, geochemistry, and geochronology of SW Mayamey granitoids. Scientific Quarterly Journal of Geosciences, 26(103): 41-60.

Sadeghian, M., 2018. Geological map of Esfeng (Scale 1:250,000). Geological Survey of Iran, Tehran.

Salami, P., Akbarpour, A., Lotfi, M., Gourabjiri, A., Mineralography, geochemistry, and Sulfur isotope study in 16B magnetite mineralization anomaly, Bafgh, Yazd. Journal of Petrology, 7 (1): 97-120 (in Persian).

Sarjoughian, F., Kananian, A., Lentz, D.R., Ahmadian, J., 2015. Nature and physicochemical conditions of crystallization in the South Dehgolan intrusion, NW Iran: mineral-chemical evidence. Turkish Journal of Earth Sciences, 24: 249-275.

Scaillet, B., Macdonald, R., 2003. Experimental constraints on the relationships between peralkaline rhyolites of the Kenya Rift Valley. Journal of Petrology, 44(13): 1867-1894.

Scaillet, B. and Macdonald, R., 2004. Fluorite stability in silicic magmas. Contributions to Mineralogy and Petrology, 147, pp.319-329. DOI: 10.1007/s00410-004-0559-1

Schmidth, M.W., 1992. Amphibole composition in tonalite as a function of pressure: an experimental calibration of the Al-in hornblende barometer. Contributions to Mineralogy and Petrology, 110: 304-310.

Sepehri-Rad, R., Alirezaei, S., Azim-Zadeh, A.M., 2018. Hydrothermal alteration in the Gazestan magnetite-apatite deposit and its comparison with other iron deposits, Bafq district, central Iran. International Journal of Geoscience, 108: 257-268.

Sepidbar, F., Ghorbani, G., Simon, A. C., Ma. J. L., Palin R. M., Homam, S. M., 2022. Formation of the Chah-Gaz iron oxide-apatite ore (IOA) deposit, Bafq District, Iran: Constraints from halogens, trace element concentrations, and Sr-Nd isotopes of fluorapatite. Ore Geology Reviews, 140: 104599, ISSN 0169-1368,

Sepidbar, F., Ghorbani, G., Zoheir, B., Palin, R. M., Homam, S. M., Zafar, T., He, L. 2021. Coeval calc-alkaline and alkaline Cadomian magmatism in the Bafq, central Iran: Insights into their petrogenesis. Lithos, 406: 106535. DOI: 10.1016/j.lithos.2021.106535

Sepidbar, F., Homam, S. M., Ghaemi, F., Stern, R. J., Jun, H., Karsli, O., Gholami, M., 2024. Cadomian tectonic evolution of Iran: records of an unusually hot and broad extensional convergent margin on the northern margin of Gondwana. International Geology Review, 66 (7): 1352-1372.

Sepidbar, F., Moghadam, H. S., Li, C., Stern, R. J., Jiantang, P., & Vesali, Y., 2020. Cadomian magmatic rocks from Zarand (SE Iran) formed in a retro-arc basin. Lithos, 366: 105569. http://dx.doi.org/10.1016/j.lithos.2020.105569

Shahri, M., 2022. Petrogenesis of metamorphic rocks in southern Iran salt domes, Southern Iran. Ph.D. Thesis, Hormozgan University Faculty of Earth Sciences, Department of Petrology, 164 p. (in Persian with English abstract).

Sharifi, A., 1997. Study of granitoids of central Iran, Esfordi-Zarigan areas. M.Sc. Thesis, Shahid University of Tehran, Faculty of Earth Sciences, 222 p. (in Persian).

Sheikh-o-leslami, B., Zamani, H., 1999. Geological map of Halvan (Scale 1:100,000). Geological Survey of Iran, Tehran. (In Persian).

Sial, A., Ferreira, V., Fallick, A., Cruz, M. J. M., 1998. Amphibole-rich clots in calc-alkalic granitoids in the Borborema province, northeastern Brazil. Journal of South American Earth Sciences, 114: 457-471. DOI: 10.1016/S0895-9811(98)00034-0

Simakin, A., Zakrevskaya, O., Salova, T., 2012. Novel amphibole geobarometer with application to Mafic Xenoliths. Earth Science Research, 1: 82-97.

Soheili, M., Mahdavi, M., 1991. Geological map of Esfordi (Scale 1:100,000). Geological Survey of

Iran, Tehran. (In Persian).
Spear, J.A., 1984. Micas in igneous rocks. In: Micas, Bailey, S.W., (ed); Mineralogical Society of America. Review in Mineralogy, 13: 299-356.
https://doi.org/10.1515/9781501508820-013
Stein, E., Dietl, C., 2001. Hornblende thermobarometry of granitoids from the Central Odenwald (Germany) and their implications for the geotectonic development of Odenwald. Mineralogy and petrology, 72: 185-207.
Stocklin, J., 1968. Structural history and tectonics of Iran: a review. American Association of Petroleum Geologists Bulletin, 52: 1229-1258.
Tyler, S.A. and Marsden, R.W., 1938. The nature of leucoxene. Journal of Sedimentary Research, 8(2): 55-58.
Teimouri, S., Ghorbani, M., Modabberi, S., 2022. Petrography and mineral chemistry of metasomatites related to Iron-Apatite mineralization in Kiruna-type deposits in the Bafq region with a focus on Choghart and Chadormalu mining district, Central Iran. Journal of crystallography and mineralogy, 30 (4):667-682 (in Persian).
Torab, F.M., Lehmann, B., 2007. Magnetite-apatite deposits of the Bafq district, Central Iran: apatite geochemistry and monazite geochronology. Mineralogical Magazine, 71(3):347-363.
Uchida, E., Endo, S., Makino, M., 2007. Relationship between solidification depth of granitic rocks and formation of hydrothermal ore deposits. Resource Geology, 57: 47-56.
Vahdati-Daneshmand, F., Zohreh-Bakhsh, A., Srdic, A., Dimitrijevic, M.N., Djokovic, I., 1992. Geological map of Rafsanjan (Scale 1: 250,000). Geological Survey of Iran, Tehran. (In Persian).
Vaziri, S.H., Majidifard, M.R., Laflamme, M., 2019. New discovery on Ediacaran fossils from the Kushk Series in Bafq and Behabad regions, Central Iran. Scientific Quarterly Journal of Geosciences, *28*(112), 261-268 (in Persian). Doi: 10.22071/gsj.2018.136508.1495
Veisskarami, M., 2018. Petrology, geochemistry and geodynamics of the Majerad metamorphic complex (southeast of Shahrood). Ph.D. Thesis, Shahrood University of Technology, Department of Petrology, 322 p. (in Persian with English abstract).
Veisskarami, M., Sadeghian, M., Ghasemi, H.A., Zhai, M., 2019. Mineral chemistry and geothermobarometry of metabasites of the igneous-metamorphic complex of Majerad (southeast of Shahrood). Journal of Economic Geology, 11: 665-684. (In Persian)
Vynhal, C.R., Mcsween, H. Y. Jr., 1991. Hornblende Chemistry in southern Appalachian granitoids: Implications for aluminous hornblende thermobarometry and magmatic epidote stability. American Mineralogist, 76: 176-188.
Zolala, F., Alipour-Asll, M., Sadeghian, M., Ghasemi, H., Zhai, M. and Amidimehr, E., 2025. Mineralogy, geochemistry, and petrogenesis of iron oxide-apatite ores in the Bafq mining district, Central Iran: Proposed a new tectonic setting for mineralization. Journal of Geochemical Exploration, 275: 107785. https://doi.org/10.1016/j.gexplo.2025.107785